Available online at www.sciencedirect.com

SCIENCE DIRECT®

Physica D 212 (2005) 271–304

PHYSICA D

www.elsevier.com/locate/physd

Definition and properties of Lagrangian coherent structures from finite-time Lyapunov exponents in two-dimensional aperiodic flows

Shawn C. Shadden[a], Francois Lekien[b,*], Jerrold E. Marsden[a]

[a] *Control and Dynamical Systems, California Institute of Technology, United States*
[b] *Mechanical and Aerospace Engineering, Princeton University, Princeton, NJ 08544, United States*

Received 24 February 2005; received in revised form 10 September 2005; accepted 13 October 2005

Communicated by U. Frisch

Abstract

This paper develops the theory and computation of Lagrangian Coherent Structures (LCS), which are defined as *ridges* of Finite-Time Lyapunov Exponent (FTLE) fields. These ridges can be seen as finite-time mixing templates. Such a framework is common in dynamical systems theory for autonomous and time-periodic systems, in which examples of LCS are stable and unstable manifolds of fixed points and periodic orbits. The concepts defined in this paper remain applicable to flows with arbitrary time dependence and, in particular, to flows that are only defined (computed or measured) over a finite interval of time.

Previous work has demonstrated the usefulness of FTLE fields and the associated LCSs for revealing the Lagrangian behavior of systems with general time dependence. However, ridges of the FTLE field need not be exactly advected with the flow. *The main result of this paper is an estimate for the flux across an LCS, which shows that the flux is small, and in most cases negligible, for well-defined LCSs or those that rotate at a speed comparable to the local Eulerian velocity field, and are computed from FTLE fields with a sufficiently long integration time*. Under these hypotheses, the structures represent nearly invariant manifolds even in systems with arbitrary time dependence.

The results are illustrated on three examples. The first is a simplified dynamical model of a double-gyre flow. The second is surface current data collected by high-frequency radar stations along the coast of Florida and the third is unsteady separation over an airfoil. In all cases, the existence of LCSs governs the transport and it is verified numerically that the flux of particles through these distinguished lines is indeed negligible.

Keywords: Coherent structures; Transport barriers; Direct and finite-time Lyapunov exponents; Mixing

---

[*] Corresponding author.
E-mail address: lekien@princeton.edu (F. Lekien).

0167-2789/$ - see front matter © 2005 Elsevier B.V. All rights reserved.
doi:10.1016/j.physd.2005.10.007

1. Introduction

Transport in dynamical systems is often studied in terms of particle trajectories in phase space [52,32]. Applied to fluids, this approach is often referred to as *Lagrangian*, in contrast to the *Eulerian* perspective where the flow is described by quantities given at fixed locations in space. Neglecting molecular diffusion, passive tracers (dye, temperature, or any other material having a negligible effect on the flow) follow fluid particle trajectories, namely curves $\mathbf{x}(t)$ in 2- or 3-space that are solutions of

$$\dot{\mathbf{x}} = \mathbf{v}(\mathbf{x}, t), \tag{1}$$

where the right-hand side is the velocity field of the fluid. Even when the velocity field has a very simple form, the behavior of the corresponding fluid trajectories can be quite complex and seemingly unpredictable, a phenomenon referred to as deterministic chaos or chaotic transport. For time-independent flows [52] and time-periodic flows [40,42], the invariant manifolds of, respectively, the fixed points and periodic orbits of the system delineate mixing templates that govern the transport of passive tracers. Useful qualitative and quantitative information about the flow can often be deduced from the intersection geometry of these invariant manifolds.

When the right-hand side of Eq. (1) has general time dependence, fixed points, periodic orbits, or other invariant sets are generally not available for defining invariant manifolds in the usual sense. Instead, one may rely on methods such as the study of uniformly hyperbolic trajectories [54,39,36] or exponential dichotomies [2,27]. However, such techniques are typically applied to analytic advection models where the behavior is known for all time. For many applications though, especially in fluid dynamics, the velocity field is only known over a finite time interval. For instance, this is typical of numerically generated flows resulting from the integration of a model or an approximation of the Navier–Stokes equations. Experimentally measured flows such as radar and satellite data also fall into this category.

It has long been recognized that flows with general time dependence admit emergent patterns which influence the transport of tracers; these structures are often generically referred to as *coherent structures*. Jones and Winkler [18] provide a recent review of available techniques and examples of transport problems in geophysical flows. When coherent structures are studied in terms of quantities derived from fluid trajectories they are often named Lagrangian coherent structures (LCS). For example, in the special case of time-independent systems, one might classify the stable and unstable manifolds of hyperbolic fixed points as coherent structures, but typically one uses the notion of coherent structures in the context of more general flows. There is a vast body of literature on coherent structures in fluid mechanics that we will not attempt to overview here. However, [26,29,11,38,18] provide many useful references on this subject and discuss some of the various approaches.

As noted by [11], in much of the literature, coherent structures are often vaguely defined, making the analysis and exact detection of such structures difficult. The motivation for the series of papers by Haller et al. [9–12] was to give a precise definition of LCS for general time-dependent systems defined, perhaps, only over a finite time interval. Haller first provided what is called a *hyperbolic time approach*, which gives a criterion for the existence of LCSs based on invariants of the gradient of the velocity field evaluated along fluid trajectories. Using this approach, LCSs are defined by local extrema of the hyperbolic time field, which measures how long each trajectory remains hyperbolic. In [12] Haller gives an alternative definition of LCS in Section 2.3 of that paper as local extrema of the finite-time Lyapunov exponent field (FTLE). He also shows the strong correspondence between LCSs computed from hyperbolicity time fields and finite-time Lyapunov exponent fields for steady and forced ABC (Arnold–Beltrami–Childress) flows.

Similar to the FTLE, which measures *how much particles separate after a given interval of time* is the FSLE (Finite-Size Lyapunov Exponent) which *measures how long it takes particles to separate to a specified distance*. The works of [20,19] demonstrate the use of FSLE for locating LCSs in atmospheric data. In this paper, we define Lagrangian Coherent Structures using finite-time Lyapunov exponent fields. A similar definition based on finite-size exponents and the comparison with the results in this paper are planned as future work.

The traditional Lyapunov exponent quantifies the *asymptotic* behavior of infinitesimally close particles in a dynamical system and their origin goes back to [25,31]. The monograph by Barreira and Pesin [1] gives a self-contained treatment of the abstract theory of Lyapunov exponents, which previously was not readily available in English. Doerner et al. [5] discussed how level contours of finite-time Lyapunov exponent fields can approximate stable manifolds for time-independent and periodic systems. In the realm of general time-dependent systems, Pierrehumbert [34] and Pierrehumbert and Yang [35] used finite-time Lyapunov exponent fields to capture chaotic mixing regions and transport barriers from atmospheric data. They used these fields to visualize the existence of structures similar to classical invariant tori that are well documented in time-periodic flows. In the paper by von Hardenberg et al. [49], a similar approach is used for studying atmospheric eddies. However, these studies did not attempt to precisely define these structures based on the finite-time Lyapunov exponent field. In this paper, we formalize the definition of LCSs as *ridges* of the finite-time Lyapunov exponent fields, a notion introduced in [14] and developed further in the present paper.

The motivation for developing a precise definition of LCS is that numerous works since the publication of [14], such as [50,23,24,17], have demonstrated the usefulness of FTLE plots and their associated LCSs for studying systems with arbitrary time dependence. However, there has remained the issue of making the Lagrangian transport properties of LCS precise. Based on previous numerical results [24], it was thought that LCSs are, at least approximately, transported as sets by the flow and so should be approximately Lagrangian. Additionally, in [12,14], LCSs as determined from FTLE fields were referred to as material lines, meaning that they should be advected by the flow. However, numerical studies have shown that ridges in the FTLE field (i.e., LCS) sometimes can exhibit non-Lagrangian behavior such as bifurcations and that they may have a small material flux. One such example can be found in [23] or at http://www.lekien.com/˜francois/papers/rsmas.

The purpose of the present paper is to fill some of the missing gaps in the question of "How Lagrangian are LCSs?". We do this by

(1) Carefully analyzing the basic definition of LCS.
(2) Deriving expressions for the exact flux across an LCS in a form that enables one to estimate its Lagrangian transport properties.
(3) Verifying and illustrating the properties on three diverse examples.

As stated above, we define LCSs as ridges in the FTLE field. Ridges are *special gradient lines of the FTLE field that are transverse to the direction of minimum curvature*. We show that for a well-defined LCS (satisfying certain non-degeneracy conditions), the flux across the structure, while not necessarily zero, is usually negligible, and therefore these structures are effectively invariant manifolds and hence act as transport barriers. In particular, for a given FTLE field which admits an LCS, we construct a scalar function $L(\mathbf{x}, t)$ such that the LCS is given by the level set $L(\mathbf{x}, t) = 0$.

A key fact, established in Section 4.3, shows that the flux across an LCS is given by

$$\Phi(t) = \int_{\mathrm{LCS}} \frac{\mathrm{d}L}{\mathrm{d}t} \mathrm{d}s. \tag{2}$$

The *main result of the paper*, given in Eq. (61) of Theorem 4.4, is the following estimate for $\mathrm{d}L/\mathrm{d}t$ based on quantities derived from the FTLE and velocity fields:

$$\frac{\mathrm{d}L}{\mathrm{d}t} = \underbrace{\frac{\langle \hat{\mathbf{t}}, \nabla\sigma \rangle}{\langle \hat{\mathbf{n}}, \Sigma\hat{\mathbf{n}} \rangle}}_{\text{term A}} \underbrace{\left\langle \hat{\mathbf{t}}, \frac{\partial \hat{\mathbf{n}}}{\partial t} - J\hat{\mathbf{n}} \right\rangle}_{\text{term B}} + \underbrace{\mathcal{O}\left(\frac{1}{|T|}\right)}_{\text{term C}}. \tag{3}$$

Ignoring, for now, the precise definition of all the quantities in the right-hand-side of Eq. (3), here is what they roughly mean: term A measures how well defined the ridge is, and goes to zero the sharper the ridge; term B represents the difference in the local rotation rate of the LCS from the local rotation rate of the Eulerian velocity field; and term C is a term which scales as $1/|T|$, where $|T|$ is the length of time over which the FTLE is computed. Therefore, for well-defined ridges or ones that rotate at a rate comparable to the local Eulerian field and are computed from a FTLE field which has a sufficiently long integration time, the flux across the LCS is expected to be small.

The purpose of the definition proposed in this paper is twofold: first, a precise definition is required to prove analytical results, and secondly, it was developed to permit computational means to extract the LCS from numerical and experimental data. An overview of a numerical algorithm to extract LCS is given and it is applied to three examples: an analytical double-gyre, observed ocean current data, and unsteady separation over an airfoil. For the first two cases, we carefully study the rate at which particles cross the LCS and find that the rate is indeed very small; in fact it is less than 0.05% of the average velocity of fluid particles near the LCS in both examples. The third example is provided to illustrate the utility of the methods presented in this paper to a wide range of applications.

2. Notation and definitions

Let the open set $D \subset \mathbb{R}^2$ be the domain of the fluid under study. Given a time-dependent velocity field $\mathbf{v}(\mathbf{x}, t)$ defined on D, define a trajectory $\mathbf{x}(t; t_0, \mathbf{x}_0)$ starting at point $\mathbf{x}_0 \in D$ at time t_0 to be the solution of

$$\begin{cases} \dot{\mathbf{x}}(t; t_0, \mathbf{x}_0) = \mathbf{v}(\mathbf{x}(t; t_0, \mathbf{x}_0), t), \\ \mathbf{x}(t_0; t_0, \mathbf{x}_0) = \mathbf{x}_0. \end{cases} \tag{4}$$

A trajectory is seen mainly as a function of time. However, its dependence on the initial position $\mathbf{x}_0$ and the initial time t_0 will be most important in this work and we want to emphasize this aspect by keeping an explicit reference to the parameters $\mathbf{x}_0$ and t_0 in the solution of Eq. (4).

In this work, we shall be making a number of basic assumptions. The first, on smoothness, is in accord with traditional assumptions in fluid mechanics [47,32]:

A1. *The velocity field* $\mathbf{v}(x, t)$ *is at least* C^0 *in time and* C^2 *in space,*

from which it follows $\mathbf{x}(t; t_0, \mathbf{x}_0)$ is C^1 in time and C^3 in space.

Fixing the initial time t_0 and the final time t, we can view the solution of the dynamical system given in Eq. (4) as a map which takes points from their position $\mathbf{x}_0$ at time t_0 to their position at time t. This map, referred to as the *flow map*, is denoted by $\phi_{t_0}^{t}$ and satisfies

$$\phi_{t_0}^{t} : D \to D : \mathbf{x}_0 \mapsto \phi_{t_0}^{t}(\mathbf{x}_0) = \mathbf{x}(t; t_0, \mathbf{x}_0). \tag{5}$$

It follows from standard theorems on *local existence and uniqueness of solutions* [16] of Eq. (4), that the map $\phi_{t_0}^{t}$ satisfies the following properties:

$$\begin{cases} \phi_{t_0}^{t_0}(\mathbf{x}) = \mathbf{x}, \\ \phi_{t_0}^{t+s}(\mathbf{x}) = \phi_{s}^{t+s}(\phi_{t_0}^{s}(\mathbf{x})) = \phi_{t}^{t+s}(\phi_{t_0}^{t}(\mathbf{x})). \end{cases} \tag{6}$$

2.1. Finite-time Lyapunov exponents

Roughly speaking, the finite-time Lyapunov exponent (FTLE) is a finite time average of the maximum expansion rate for a pair of particles advected in the flow. For example, consider a point located at $\mathbf{x} \in D$ at time t_0. When advected, this point moves to $\phi_{t_0}^{t_0+T}(\mathbf{x})$ after a time interval T. To understand the amount of stretching about this trajectory, consider the evolution of the perturbed point $\mathbf{y} = \mathbf{x} + \delta\mathbf{x}(0)$ where $\delta\mathbf{x}(0)$ is infinitesimal and, for now, arbitrarily oriented. After a time interval T, this perturbation becomes

$$\delta\mathbf{x}(T) = \phi_{t_0}^{t_0+T}(\mathbf{y}) - \phi_{t_0}^{t_0+T}(\mathbf{x}) = \frac{\mathrm{d}\phi_{t_0}^{t_0+T}(\mathbf{x})}{\mathrm{d}\mathbf{x}}\delta\mathbf{x}(0) + \mathcal{O}(\|\delta\mathbf{x}(0)\|^2). \tag{7}$$

This equation employs the *Landau* notation [28]; that is, $f(x) = \mathcal{O}(g)$ for a positive function g means that $f(x)/g(x)$ remains bounded for all $x \in \mathbb{R}$. The growth of linearized perturbations are obtained by dropping the $\mathcal{O}(\|\delta\mathbf{x}(0)\|^2)$ terms, and so using the standard Euclidean norm, the magnitude of the perturbation is given by

$$\|\delta\mathbf{x}(T)\| = \sqrt{\left\langle \delta\mathbf{x}(0), \frac{\mathrm{d}\phi_{t_0}^{t_0+T}(\mathbf{x})}{\mathrm{d}\mathbf{x}}^{*} \frac{\mathrm{d}\phi_{t_0}^{t_0+T}(\mathbf{x})}{\mathrm{d}\mathbf{x}}\delta\mathbf{x}(0)\right\rangle} \tag{8}$$

where M^* denotes the adjoint (transpose) of M. The symmetric matrix

$$\Delta = \frac{\mathrm{d}\phi_{t_0}^{t_0+T}(\mathbf{x})}{\mathrm{d}\mathbf{x}}^{*} \frac{\mathrm{d}\phi_{t_0}^{t_0+T}(\mathbf{x})}{\mathrm{d}\mathbf{x}} \tag{9}$$

is a *finite-time* version of the (right) Cauchy–Green deformation tensor. Although Δ is a function of $\mathbf{x}$, t_0, and T, we suppress writing these explicit dependencies to avoid notational clutter.

Maximum stretching occurs when $\delta\mathbf{x}(0)$ is chosen such that it is aligned with the eigenvector associated with the maximum eigenvalue of Δ. That is, if $\lambda_{\max}(\Delta)$ is the maximum eigenvalue of Δ, thought of as an operator, then

$$\max_{\delta\mathbf{x}(0)} \|\delta\mathbf{x}(T)\| = \sqrt{\lambda_{\max}(\Delta)}\|\overline{\delta\mathbf{x}}(0)\| \tag{10}$$

where $\overline{\delta\mathbf{x}}(0)$ is aligned with the eigenvector associated with $\lambda_{\max}(\Delta)$. Then, Eq. (10) can be recast as

$$\max_{\delta\mathbf{x}(0)} \|\delta\mathbf{x}(T)\| = \mathrm{e}^{\sigma_{t_0}^{T}(\mathbf{x})|T|}\|\overline{\delta\mathbf{x}}(0)\|, \tag{11}$$

where

$$\sigma_{t_0}^{T}(\mathbf{x}) = \frac{1}{|T|}\ln\sqrt{\lambda_{\max}(\Delta)}. \tag{12}$$

Eq. (12) represents the (largest) finite-time Lyapunov exponent with a finite integration time T, which is associated to point $\mathbf{x} \in D$ at time t_0. Notice that the absolute value of the integration time is used in Eq. (12). This work permits both positive and negative integration times T. Earlier work [13] motivates the use of backward-time integration for locating *attracting Lagrangian coherent structures* (e.g., unstable manifolds for time-independent vector fields), and forward-time integration for revealing *repelling Lagrangian coherent structures* (e.g., stable manifolds for time-independent vector fields). For brevity, we often refer to the FTLE as just $\sigma(\mathbf{x})$, or more simply σ, when the extra notation can be dropped without causing ambiguity.

Early work in the area of Lyapunov exponents [31] motivates the importance of restricting the study to flows satisfying the following condition:

A2. *There is a constant k such that*

$$\left\|\frac{\mathrm{d}\phi_{t_0}^{t}(\mathbf{x})}{\mathrm{d}\mathbf{x}}\right\| \le \mathrm{e}^{k|t-t_0|}, \tag{13}$$

for all t.

This assumption is reasonable assuming the velocity field is Lipschitz continuous, cf. Thm. 1.4 of [48].

In this paper, we restrict the domain of the fluid D to be a subset of $\mathbb{R}^2$. There is no conceptual problem with working in higher dimensions, but the definitions and analysis presented in this paper become somewhat more complicated.

In this work, we are concerned with trajectories that satisfy the property:

$$\textbf{A3.}\quad \ln\lambda_{\min}(\Delta) < 0 < \ln\lambda_{\max}(\Delta). \tag{14}$$

Notice that for finite T, Δ measures the average deformation of a perturbation over the interval T. So for instance, if an (infinitesimal) circular blob of particles is placed about a trajectory that satisfies **A3**, then after an amount of time T, the blob will have expanded in one direction and compressed in the other to form an elliptical shape. We refer to such trajectories as finite-time hyperbolic [53].

If we were to take $T \to \infty$, we should assume that there exist arbitrary constants $\mu_{\min}$ and $\mu_{\max}$ such that the eigenvalues satisfy

$$\ln\lambda_{\min}(\Delta) \le \mu_{\min} < 0 < \mu_{\max} \le \ln\lambda_{\max}(\Delta), \tag{15}$$

so that the logarithms of the eigenvalues are uniformly bounded away from zero. For the sort of examples of interest in this paper, the dynamical system is only defined on a finite interval of time and therefore, to consider $T \to \infty$, we can follow [18] and assume that the finite-time field is extended using bump functions. In this case, uniform boundedness is equivalent to boundedness. In other words, this uniform boundedness property is not a problem in the finite-time context.

All trajectories satisfying Eq. (14) are contained within an open set (not necessarily connected) of the extended phase space $D \times \mathbb{R}$. In the rest of this work, we assume that everything is done in this subset only. This restriction allows us to work only in regions where the Lagrangian Coherent Structures are codimension-1 manifolds. Hyperbolic trajectories for which the logarithm of both eigenvalues of the Cauchy–Green deformation tensor have the same sign correspond to *areas* of expansion or compression (source/sinks). These regions are of less importance in studying the Lagrangian barrier properties of the flow because there is no codimension-1 structure separating regions of different dynamics.

As mentioned in [11,14,49], flows that have lines of high shear can produce particle separation plots (e.g., FTLE fields) which will have ridges along the shear lines. The problem with this is that it is then hard to distinguish lines of high shear from "hyperbolic lines", i.e., lines about which there is exponential stretching orthogonal to the line. Assumption **A3** precludes lines of pure shear and hence this paper does not address the properties of LCSs that result from such behavior.

Lemma 2.1. *The field* $\sigma_{t_0}^{T}(\mathbf{x})$ *is* C^2 *in space and* C^1 *in time.*

Proof. Since $\phi_{t_0}^{t_0+T}(\mathbf{x})$ is a C^3 in space (C^1 in time) diffeomorphism, the Cauchy–Green deformation tensor Δ is C^2 in space (C^1 in time) and invertible. Since Eq. (14) requires that the two eigenvalues are distinct, they are also C^2 in space (C^1 in time) functions. Also, Δ is a real symmetric matrix, so its two eigenvalues are real and positive. Hence the logarithm of the largest eigenvalue is C^2 in space and C^1 in time. □

2.2. Ridges and LCS

FTLE fields for a wide variety of flows reveal distinguished lines of high FTLE. While detecting these structures is usually obvious by inspection, an exact definition is required to facilitate proving properties of the structures and for building efficient numerical algorithms to extract these curves. For a FTLE field, $\sigma_{t_0}^{T}(\mathbf{x})$, we define Lagrangian Coherent Structures as *ridges* of the field. In this section, we make this definition precise.

As a small point, from a geometric point of view, a ridge of an arbitrary surface should lie *within* that surface. However, for our application we are concerned with extracting ridges of the *graph* of the function

$\sigma : D \subset \mathbb{R}^2 \to \mathbb{R}$, where the graph is thought of as a surface in $\mathbb{R}^3$. Since the motion of the fluid is confined to the domain $D \subset \mathbb{R}^2$, it only makes sense to define the parametrization of the ridge over D, that is, the ridge lies within the domain D and not within the graph of σ.

Below, we give two alternative, but similar, definitions of a ridge, the first being a *curvature ridge* of an FTLE field. Key concepts in this geometric definition are that of principal curvatures and principal directions [30]. Our definition of a curvature ridge can easily be generalized for an arbitrary orientable surface. We then present a more convenient and somewhat simpler definition of a ridge known as a *second-derivative ridge*, which does not rely on the geometric notions of principal curvatures and directions, but instead on Σ, the Hessian of the FTLE field, i.e.,

$$\Sigma = \frac{\mathrm{d}^2\sigma_{t_0}^T(\mathbf{x})}{\mathrm{d}\mathbf{x}^2}. \tag{16}$$

It is instructive to keep in mind the intuition behind each definition. For example, if hiking along a “ridge” one would expect (1) to be *locally* at the highest point in the field transverse to the ridge, that is, if the hiker stepped to the right or left of the path, they would be stepping down, and (2) for the topography to drop off steepest in the direction transverse to the ridge, that is, at each point on the ridge, the direction the topography decreases most rapidly should be transverse to the ridge. The two definitions below formally state these two conditions; however, they differ in the reference direction they use for “down”. In the first definition, the downward direction is always parallel to the normal vector field of the graph, whereas in the second definition, the downward direction is fixed and points toward the xy-plane.[1]

Definition 2.1. Let $\mathcal{G} \subset \mathbb{R}^3$ denote the graph of $\sigma : D \subset \mathbb{R}^2 \to \mathbb{R}$. Let $\pi : \mathcal{G} \to D$ be the standard projection map, with its associated tangent map $T\pi$. A **curvature ridge** of the graph $\mathcal{G}$ is an injective curve $\mathbf{c} : (a, b) \to D$, satisfying the following conditions for each s in the open interval (a, b):

CR1. The vectors $\mathbf{c}'(s) = \frac{\mathrm{d}\mathbf{c}}{\mathrm{d}s}$ and $\nabla\sigma(\mathbf{c}(s))$ are parallel.

CR2. Regard $\mathcal{G}$ as an orientated surface in $\mathbb{R}^3$. Let $\mathbf{p} = \mathbf{c}(s)$ and $\tilde{\mathbf{p}} = \pi^{-1}(\mathbf{p}) \in \mathcal{G}$. Let $k^u_{\tilde{\mathbf{p}}}$ and $k^l_{\tilde{\mathbf{p}}}$ denote the maximum and minimum principal curvatures of $\mathcal{G}$ at the point $\tilde{\mathbf{p}}$ with corresponding unit principal vectors $\tilde{\mathbf{u}}^u_{\tilde{\mathbf{p}}}$ and $\tilde{\mathbf{u}}^l_{\tilde{\mathbf{p}}}$. We require that $k^l_{\tilde{\mathbf{p}}} < 0$ and that $T\pi(\tilde{\mathbf{u}}^l_{\tilde{\mathbf{p}}})$ be normal to $\mathbf{c}'(s)$.

Definition 2.2. A **second-derivative ridge** of σ is an injective curve $\mathbf{c} : (a, b) \to D$ satisfying the following conditions for each $s \in (a, b)$:

SR1. The vectors $\mathbf{c}'(s)$ and $\nabla\sigma(\mathbf{c}(s))$ are parallel.

SR2. $\Sigma(\mathbf{n}, \mathbf{n}) = \min_{\|\mathbf{u}\|=1} \Sigma(\mathbf{u}, \mathbf{u}) < 0$, where $\mathbf{n}$ is a unit normal vector to the curve $\mathbf{c}(s)$ and Σ is thought of as a bilinear form evaluated at the point $\mathbf{c}(s)$.

Since the FTLE field, $\sigma_t^T(\mathbf{x})$, varies with time, t, it is often convenient to append a subscript on $\mathbf{c}(s)$ to refer to the time at which the FTLE is computed. Therefore, we write $\mathbf{c}_t(s)$ for a ridge in the FTLE field at time t. The objective of this paper is to investigate how ridges of the FTLE field evolve over time. In particular, our goal is to show that $\mathbf{c}_t(s)$ behaves approximately like a line of Lagrangian particles, i.e., a *material line*, when t is varied.

Theorem 2.1. *The curves* $\mathbf{c}(s)$ *given in the above definitions are* C^2.

Proof. By Lemma 2.1, $\nabla\sigma(\mathbf{c}(s))$ is C^1. By **SR2**, $\mathbf{c}'(s)$ is necessarily parallel to $\nabla\sigma(\mathbf{c}(s))$, hence we can always find a parametrization such that $\mathbf{c}'(s)$ is C^1, which implies that $\mathbf{c}(s)$ is C^2. □

---

[1] We assume $D \subset xy$-plane.

The main difference between the two definitions lies in the following: in **CR2** the curvature is measured with respect to the tangent plane to the graph of σ at each point, whereas in **SR2**, the curvature is always with respect to the xy-plane. The first definition is more intrinsic, whereas the second is more intuitive. As expected, one can prove the two measures are equal at local extrema, at which the two planes are parallel. In the next section, we show that a second-derivative ridge is always a subset of a curvature ridge.

2.3. Equivalence between ridges

The relationships between the curvature measures used in the two previous definitions can be summarized as follows.

Theorem 2.2. *For each point* $\mathbf{p} \in D$, *let* $\mathbf{t}$ *be a vector of arbitrary length oriented along* $\nabla\sigma$ *and* $\mathbf{n}$ *be a vector of arbitrary length oriented orthogonal to* $\mathbf{t}$ *(if* $\nabla\sigma = 0$, $\mathbf{t}$ *can be arbitrarily oriented). Let* $\gamma_n = \Sigma(\mathbf{n}, \mathbf{n})$ *and* $\gamma_t = \Sigma(\mathbf{t}, \mathbf{t})$. *As before, let* $\tilde{\mathbf{t}} = (T\pi)^{-1}\mathbf{t}$ *and* $\tilde{\mathbf{n}} = (T\pi)^{-1}\mathbf{n}$. *Then we have the following relations:*

$$\gamma_n = \kappa k(\tilde{\mathbf{n}})$$
$$\gamma_t = \kappa^3 k(\tilde{\mathbf{t}}),$$

where

$$\kappa = \sqrt{1 + \left(\frac{\partial\sigma}{\partial x}\right)^2 + \left(\frac{\partial\sigma}{\partial y}\right)^2}.$$

Proof. Let the FTLE field be given by the function $\sigma(x, y)$ and $\mathcal{G}$ denote the graph $z = \sigma(x, y)$. The unit normal field to $\mathcal{G}$ is given by

$$\mathbf{u} = \frac{1}{\kappa}\left(-\frac{\partial\sigma}{\partial x}, -\frac{\partial\sigma}{\partial y}, 1\right). \tag{17}$$

By definition [30], the normal curvature in the direction $\tilde{\mathbf{n}}$ is given by

$$k(\tilde{\mathbf{n}}) = \tilde{\mathbf{n}} \cdot \nabla_{\tilde{\mathbf{n}}}\mathbf{u} \tag{18}$$

where $\nabla_{\tilde{\mathbf{n}}}\mathbf{u}$ is the covariant derivative of $\mathbf{u}$ with respect to $\tilde{\mathbf{n}}$.

Using the preceding formula for an arbitrary vector $\mathbf{w} = (w_x, w_y, w_z)$, the curvature along $\mathbf{w}$ is given by

$$\begin{aligned} k(\mathbf{w}) \; = \; & \frac{1}{\kappa}\left(w_x^2\frac{\partial^2\sigma}{\partial x^2} + 2w_x w_y\frac{\partial^2\sigma}{\partial x\partial y} + w_y^2\frac{\partial^2\sigma}{\partial y^2}\right) \\ & - \frac{1}{\kappa^3}\left(\frac{\partial\sigma}{\partial x}\left(\frac{\partial\sigma}{\partial x}\frac{\partial^2\sigma}{\partial x\partial y} + \frac{\partial\sigma}{\partial y}\frac{\partial^2\sigma}{\partial y^2}\right) + \frac{\partial\sigma}{\partial y}\left(\frac{\partial\sigma}{\partial y}\frac{\partial^2\sigma}{\partial x\partial y} + \frac{\partial\sigma}{\partial x}\frac{\partial^2\sigma}{\partial x^2}\right)\right)w_x w_y \\ & - \frac{1}{\kappa^3}\left(\frac{\partial\sigma}{\partial x}\left(\frac{\partial\sigma}{\partial y}\frac{\partial^2\sigma}{\partial x\partial y} + \frac{\partial\sigma}{\partial x}\frac{\partial^2\sigma}{\partial x^2}\right)w_x^2 + \frac{\partial\sigma}{\partial y}\left(\frac{\partial\sigma}{\partial x}\frac{\partial^2\sigma}{\partial x\partial y} + \frac{\partial\sigma}{\partial y}\frac{\partial^2\sigma}{\partial y^2}\right)w_y^2\right). \end{aligned} \tag{19}$$

Plugging in $\tilde{\mathbf{n}}$ for $\mathbf{w}$ in Eq. (19) and using the fact that

$$\nabla\sigma \cdot \mathbf{n} = 0, \tag{20}$$

we get

$$k(\tilde{\mathbf{n}}) = \frac{1}{\kappa}\left(n_x^2\frac{\partial^2\sigma}{\partial x^2} + 2n_x n_y\frac{\partial^2\sigma}{\partial x\partial y} + n_y^2\frac{\partial^2\sigma}{\partial y^2}\right) = \frac{1}{\kappa}\Sigma(\mathbf{n}, \mathbf{n}). \tag{21}$$

Now let $\tilde{\mathbf{t}} = \mathbf{u} \times \tilde{\mathbf{n}}$. As above, define

$$k(\tilde{\mathbf{t}}) = \tilde{\mathbf{t}} \cdot \nabla_{\tilde{\mathbf{t}}} \mathbf{u}. \tag{22}$$

If $k(\tilde{\mathbf{t}})$ is expanded out and reduced, some algebra shows that

$$k(\tilde{\mathbf{t}}) = \frac{1}{\kappa^3} \left(t_x^2 \frac{\partial^2 \sigma}{\partial x^2} + 2 t_x t_y \frac{\partial^2 \sigma}{\partial x \partial y} + t_y^2 \frac{\partial^2 \sigma}{\partial y^2} \right) = \frac{1}{\kappa^3} \Sigma(\mathbf{t}, \mathbf{t}). \quad \square \tag{23}$$

Notice that $\kappa \geq 1$. Therefore, equality of the two curvature measures holds when $\kappa = 1$, which implies that $\nabla \sigma = 0$ (i.e., the tangent plane of $\mathcal{G}$ is parallel to the xy-plane).

Theorem 2.3. *A second derivative ridge is always identical to or a subset of a curvature ridge.*

Proof. We must show that all points along a second-derivative ridge satisfy the conditions of a curvature ridge. Notice that **CR1** is trivially satisfied if **SR1** is true. Hence we must show **CR2**, that is, $k(\tilde{\mathbf{n}})$ is a minimum and less than zero, where $\tilde{\mathbf{n}}$ is the lift of $\mathbf{n}$, and $\mathbf{n}$ satisfies **SR2**, i.e.,

$$\Sigma(\mathbf{n}, \mathbf{n}) = \min_{\|\mathbf{u}\|=1} \Sigma(\mathbf{u}, \mathbf{u}) < 0 \tag{24}$$

with $\mathbf{n}$ orthogonal to $\nabla \sigma$.

From Theorem 2.2, $k(\tilde{\mathbf{n}})$ is necessarily less than zero if Eq. (24) is satisfied. Thus, it is left to show that $k(\tilde{\mathbf{n}})$ is minimized in the (lifted) direction orthogonal to the second-derivative ridge. It should be clear that the scaling introduced in Theorem 2.2 will not affect the difference in ridge definitions for all points in which Σ has a non-negative eigenvalue. Therefore, assume that the eigenvalues of Σ satisfy $\lambda_{\min} < \lambda_{\max} < 0$. Without loss of generality we can assume the second-derivative ridge is locally aligned with the x-axis, i.e., that $\frac{\partial \sigma}{\partial y} = 0$. This, along with Eq. (24), puts Σ in canonical form

$$\Sigma = \begin{bmatrix} \lambda_{\max} & 0 \\ 0 & \lambda_{\min} \end{bmatrix}. \tag{25}$$

Using this relation in Eq. (19) gives

$$k(\hat{\mathbf{u}}) = \frac{1}{\kappa} (u_x^2 \lambda_{\max} + u_y^2 \lambda_{\min}) - \frac{1}{\kappa^3} (|\nabla \sigma|^2 \lambda_{\max} u_x^2) \tag{26}$$

for an arbitrary unit vector $\hat{\mathbf{u}} = (u_x, u_y, 0)$. Notice that both terms in Eq. (26) are positive, hence $k(\hat{\mathbf{u}})$ is minimized if $\hat{\mathbf{u}}$ is in the y-direction (i.e., $\hat{\mathbf{u}} = (0, 1, 0)$), which is the direction orthogonal to the second-derivative ridge. $\square$

2.4. Example

Here we present an example to demonstrate the notions of curvature ridges and second-derivative ridges. Panels (a) and (b) of Fig. 1 show the graph of an analytical test field σ. It seems intuitive to call the line $y = 0$ a ridge except along the "valley" of the graph, centered around the point (2, 0) in the domain.

It is easily verified that **CR1**, and hence **SR1**, is satisfied for the line $y = 0$. The principal curvatures and second-derivative values given in **CR2** and **SR2** are plotted in Panel (c) of Fig. 1. Panel (d) of Fig. 1 shows a close-up around the value $x = 1.2$. Notice that **SR2** is satisfied for all x less than $x \approx 1.195$ (i.e., up to the second-derivative curvature intersection point shown in Panel (d)) whereas **CR2** is satisfied for all x less than $x \approx 1.2$ (i.e., up to the principal curvature intersection point shown on Panel (d) of Fig. 1). Therefore we see that the second-derivative ridge is a subset of the curvature ridge, which is of course in agreement with Theorem 2.3. In addition, this example shows how the two measures produce near identical results in this case.

The functional form for σ in this example was chosen to produce an interesting test-case. For actual FTLE fields, σ typically does not vary much along the ridges of the field—in fact, much less than shown in this example.

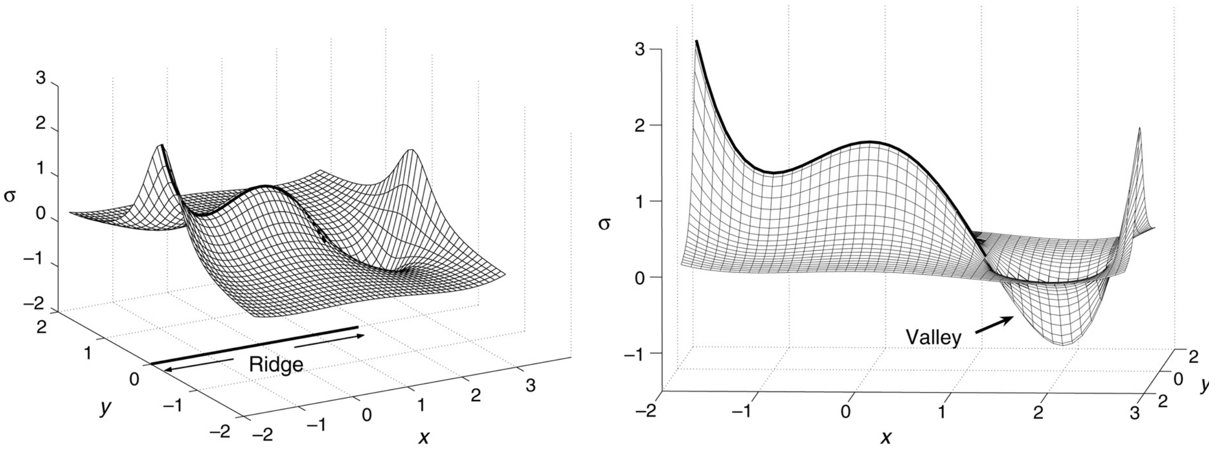

(a) $\sigma = \frac{3x^4-4x^3-12x^2+18}{12(1+4y^2)}$.

(b) Side view.

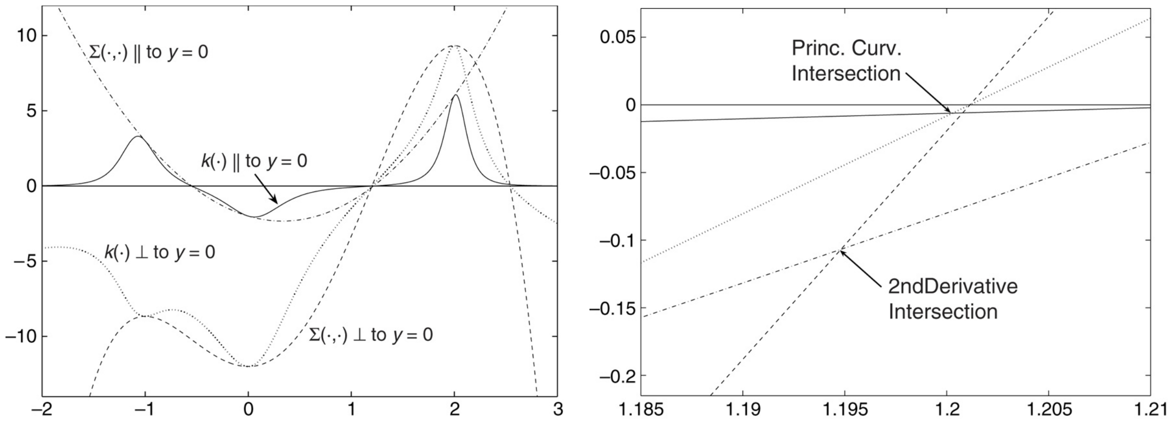

(c) Curvature measures evaluated along the x-axis (i.e., $y = 0$).

(d) Close-up.

Fig. 1. Comparison between ridge definitions. Notice that the second-derivative ridge is slightly shorter than the curvature ridge.

Therefore we can expect the difference between the two measures to be identically zero or non-existent for all practical purposes. For autonomous systems, σ is constant along a ridge (asymptotically), hence the two definitions of ridge are always identical for such systems.

2.5. Lagrangian coherent structures

Given the graph of a function, the Hessian only represents the curvature of the graph at local extrema, therefore defining a ridge in terms of principal curvatures gives a better physical interpretation and is more intrinsic. However, the notion of a second-derivative ridge is somewhat simpler and more convenient, as we shall see later in this work. Also, we have shown that a second-derivative ridge is always a subset of a principal curvature ridge, and moreover the two definitions are nearly identical for all practical purposes. In addition, the second-derivative definition facilitates computational implementation. Therefore, we define LCS as follows:

Definition 2.3. At each time t, a **Lagrangian Coherent Structure** (LCS) is a second-derivative ridge of the scalar field $\sigma_t^T(\mathbf{x})$.

As mentioned in the Introduction, it is well known that LCS can reveal an underlying flow structure in time-dependent systems that is typically not evident from the Eulerian field. In addition, these structures divide dynamically distinct regions in the flow, which allow for the easy analysis of transport. However, it is not clear from their definition that LCSs are *material lines*. We shall address this issue in Section 4.

Recall that the FTLE field, $\sigma_t^T(\mathbf{x})$, is a Lagrangian measure over a *finite* interval of time. Therefore, we might expect the flux over an LCS to be inversely proportional to the integration time T. Also, we might expect that sharp, well-defined ridges are more Lagrangian than poorly defined ridges. Both parts of this intuition turn out to be true and are made precise in Section 4 where we derive a formula for the flux across the LCS and later show that in many interesting cases the flux is negligible. In the next section, we evaluate the Lagrangian properties of the FTLE field itself.

3. Lagrangian FTLE field

In this section we show that the finite-time Lyapunov exponent, $\sigma_t^T(\mathbf{x})$, is Lagrangian in the limit of large integration times T. Notice that this does not guarantee that the LCSs are Lagrangian; they rely on higher derivatives of σ or on its curvature which are generally not Lagrangian.

For an arbitrary 2×2 matrix, A, the natural matrix norm induced from the L_2-norm on $\mathbb{R}^2$ is defined as the largest eigenvalue of the matrix $\sqrt{A^*A}$. Therefore, the definition of $\sigma_t^T(\mathbf{x})$ can be conveniently recast as

$$\sigma_{t_0}^T(\mathbf{x}) = \frac{1}{|T|} \ln \left\| \frac{\mathrm{d}\phi_{t_0}^{t+T}(\mathbf{x})}{\mathrm{d}\mathbf{x}} \right\|. \tag{27}$$

Recalling that the traditional Lyapunov exponent is defined by Eq. (27) for $T \to \infty$, we then have:

Theorem 3.1. *The traditional Lyapunov exponent is constant along trajectories.*

This theorem could be restated as: *The finite-time Lyapunov exponent becomes constant along trajectories for large integration times T.*

Proof. We compare the value of the Lyapunov exponent computed at two different points of the same trajectory. Without loss of generality, we assume that the initial time is $t_0 = 0$. Let $\mathbf{y} = \phi_0^s(\mathbf{x})$ for some arbitrary, but fixed, $s \in \mathbb{R}$. We have

$$\begin{aligned}
|T|(\sigma_0^T(\mathbf{x}) - \sigma_s^T(\mathbf{y})) &= \ln \left\| \frac{\mathrm{d}\phi_0^T(\mathbf{x})}{\mathrm{d}\mathbf{x}} \right\| - \ln \left\| \frac{\mathrm{d}\phi_s^{s+T}(\mathbf{y})}{\mathrm{d}\mathbf{y}} \right\| \\
&= \ln \left\| \frac{\mathrm{d}(\phi_{T+s}^T(\phi_T^{T+s}(\phi_s^T(\phi_0^s(\mathbf{x})))))}{\mathrm{d}\mathbf{x}} \right\| - \ln \left\| \frac{\mathrm{d}(\phi_T^{s+T}(\phi_s^T(\mathbf{y})))}{\mathrm{d}\mathbf{y}} \right\| \\
&= \ln \left\| \frac{\mathrm{d}\phi_{T+s}^T(\hat{\mathbf{y}})}{\mathrm{d}\hat{\mathbf{y}}} \frac{\mathrm{d}\phi_T^{T+s}(\hat{\mathbf{x}})}{\mathrm{d}\hat{\mathbf{x}}} \frac{\mathrm{d}\phi_s^T(\mathbf{y})}{\mathrm{d}\mathbf{y}} \frac{\mathrm{d}\phi_0^s(\mathbf{x})}{\mathrm{d}\mathbf{x}} \right\| - \ln \left\| \frac{\mathrm{d}\phi_T^{s+T}(\hat{\mathbf{x}})}{\mathrm{d}\hat{\mathbf{x}}} \frac{\mathrm{d}\phi_s^T(\mathbf{y})}{\mathrm{d}\mathbf{y}} \right\| \\
&\le \ln \left(\left\| \frac{\mathrm{d}\phi_{T+s}^T(\hat{\mathbf{y}})}{\mathrm{d}\hat{\mathbf{y}}} \right\| \left\| \frac{\mathrm{d}\phi_T^{T+s}(\hat{\mathbf{x}})}{\mathrm{d}\hat{\mathbf{x}}} \frac{\mathrm{d}\phi_s^T(\mathbf{y})}{\mathrm{d}\mathbf{y}} \right\| \left\| \frac{\mathrm{d}\phi_0^s(\mathbf{x})}{\mathrm{d}\mathbf{x}} \right\| \right) - \ln \left\| \frac{\mathrm{d}\phi_T^{s+T}(\hat{\mathbf{x}})}{\mathrm{d}\hat{\mathbf{x}}} \frac{\mathrm{d}\phi_s^T(\mathbf{y})}{\mathrm{d}\mathbf{y}} \right\| \\
&= \ln \left\| \frac{\mathrm{d}\phi_{T+s}^T(\hat{\mathbf{y}})}{\mathrm{d}\hat{\mathbf{y}}} \right\| + \ln \left\| \frac{\mathrm{d}\phi_0^s(\mathbf{x})}{\mathrm{d}\mathbf{x}} \right\| \le 2k|s|,
\end{aligned}$$

where we have used properties of the flow map given in Eq. (6) and the maximum exponential stretching hypothesis of Eq. (13). Similarly,

$$\begin{aligned}
|T|\left(\sigma_s^T(\mathbf{y})-\sigma_0^T(\mathbf{x})\right) &= \ln\left\|\frac{\mathrm{d}\phi_s^{s+T}(\mathbf{y})}{\mathrm{d}\mathbf{y}}\right\| - \ln\left\|\frac{\mathrm{d}\phi_0^T(\mathbf{x})}{\mathrm{d}\mathbf{x}}\right\| \\
&= \ln\left\|\frac{\mathrm{d}(\phi_T^{s+T}(\phi_0^T(\phi_s^0(\mathbf{y}))))}{\mathrm{d}\mathbf{y}}\right\| - \ln\left\|\frac{\mathrm{d}(\phi_0^T(\mathbf{x}))}{\mathrm{d}\mathbf{x}}\right\| \\
&= \ln\left\|\frac{\mathrm{d}\phi_T^{s+T}(\hat{\mathbf{x}})}{\mathrm{d}\hat{\mathbf{x}}}\frac{\mathrm{d}\phi_0^T(\mathbf{x})}{\mathrm{d}\mathbf{x}}\frac{\mathrm{d}\phi_s^0(\mathbf{y})}{\mathrm{d}\mathbf{y}}\right\| - \ln\left\|\frac{\mathrm{d}\phi_0^T(\mathbf{x})}{\mathrm{d}\mathbf{x}}\right\| \\
&\le \ln\left(\left\|\frac{\mathrm{d}\phi_T^{s+T}(\hat{\mathbf{x}})}{\mathrm{d}\hat{\mathbf{x}}}\right\|\left\|\frac{\mathrm{d}\phi_0^T(\mathbf{x})}{\mathrm{d}\mathbf{x}}\right\|\left\|\frac{\mathrm{d}\phi_s^0(\mathbf{y})}{\mathrm{d}\mathbf{y}}\right\|\right) - \ln\left\|\frac{\mathrm{d}\phi_0^T(\mathbf{x})}{\mathrm{d}\mathbf{x}}\right\| \\
&= \ln\left\|\frac{\mathrm{d}\phi_T^{s+T}(\hat{\mathbf{x}})}{\mathrm{d}\hat{\mathbf{x}}}\right\| + \ln\left\|\frac{\mathrm{d}\phi_s^0(\mathbf{y})}{\mathrm{d}\mathbf{y}}\right\| \le 2k|s|,
\end{aligned}$$

so we have

$$\|\sigma_0^T(\mathbf{x})-\sigma_s^T(\mathbf{y})\| \le 2k\frac{|s|}{|T|}. \tag{28}$$

Therefore

$$\left\|\frac{\mathrm{d}\sigma_t^T(\mathbf{x})}{\mathrm{d}t}\right\| = \lim_{s\to 0}\frac{\|\sigma_{t+s}^T(\mathbf{y})-\sigma_t^T(\mathbf{x})\|}{|s|} \le \frac{2k}{|T|} = \mathcal{O}(1/|T|). \tag{29}$$

Taking the limit as $|T|\to\infty$ gives

$$\limsup_{|T|\to\infty}\left\|\frac{\mathrm{d}\sigma_t^T(\mathbf{x})}{\mathrm{d}t}\right\| = 0, \tag{30}$$

which implies

$$\lim_{|T|\to\infty}\left\|\frac{\mathrm{d}\sigma_t^T(\mathbf{x})}{\mathrm{d}t}\right\| = 0. \quad \Box \tag{31}$$

The following Corollary provides a bound on the variation of $\nabla\sigma$ in time.

Corollary 3.1. *We have*

$$\frac{\partial\nabla\sigma}{\partial t} = -J^*\nabla\sigma - \Sigma\mathbf{v} + \mathcal{O}(1/|T|), \tag{32}$$

where J is the Jacobian matrix of the velocity field $\mathbf{v}$.

Proof. From Eq. (29), the material derivative of σ satisfies

$$\frac{\mathrm{d}}{\mathrm{d}t}\sigma_t^T(\mathbf{x}) = \mathcal{O}(1/|T|).$$

As a result,

$$\frac{\partial\sigma}{\partial t} = -\langle\mathbf{v},\nabla\sigma\rangle + \mathcal{O}(1/|T|). \tag{33}$$

Lemma 2.1 guarantees that $\nabla\sigma$ is C^1 in time. Therefore, we have $|\frac{\partial\nabla\sigma}{\partial t}| < \infty$ and the (spatial) derivative of Eq. (33) yields

$$\frac{\partial\nabla\sigma}{\partial t} = \nabla\frac{\partial\sigma}{\partial t} = -J^*\nabla\sigma - \Sigma\mathbf{v} + \mathcal{O}(1/|T|). \quad \square \tag{34}$$

We will use Corollary 3.1 in the next section to derive an estimate for the flux across an LCS. Notice that although Σ is technically a bilinear form, in Corollary 3.1 we made use of Riesz's representation theorem and represented Σ as a linear operator by defining $\Sigma\mathbf{u}$ (for any $\mathbf{u}$) as the unique vector that satisfies

$$\langle\mathbf{v}, \Sigma\mathbf{u}\rangle = \Sigma(\mathbf{v}, \mathbf{u}), \tag{35}$$

for all $\mathbf{v}$. This will be encountered again for Σ and similar bilinear forms when needed.

4. Lagrangian ridges

The purpose of this section is to derive the flux through an LCS based only on the geometry of the FTLE field and the given dynamical system. To simplify the derivations, in Section 4.1 we define a function $L(\mathbf{x}, t)$ such that the LCS is given by the level set $L(\mathbf{x}, t) = 0$. Some useful properties of $L(\mathbf{x}, t)$ and its derivatives are then derived in Section 4.2, including an expression for $\mathrm{d}L/\mathrm{d}t$ given in Eq. (61). We show that the infinitesimal flux at any point on the LCS is given by

$$\mathrm{d}\Phi = \left.\frac{\mathrm{d}L}{\mathrm{d}t}\right|_{L=0} \mathrm{d}s$$

where $\mathrm{d}s$ is the infinitesimal arc length along the LCS and the right-hand side is to be replaced with Eq. (61), which contains values that can be obtained from the geometry of the FTLE field and the dynamical system. We then analyze and discuss the interpretation of this estimate in Section 4.3.

4.1. Representation

Suppose that we are given an FTLE field, $\sigma_t^T(\mathbf{x})$ for $t \in [t_1, t_2]$ which admits an LCS in the sense of Definition 2.3. We define a scalar function L of space and time as follows:

Definition 4.1. For every time t, let $L(\mathbf{x}, t)$ be the function of $\mathbf{x} \in D$ defined by the conditions

1. $|L(\mathbf{x}, t)| = \|\mathbf{x} - \mathbf{x}_q\|$, where $\mathbf{x}_q$ is the point on the closure of the path representing the LCS closest to the point $\mathbf{x}$.
2. $L(\mathbf{x}, t)(((\mathbf{x} - \mathbf{x}_q) \times \mathbf{c}_t'(s)) \cdot \hat{\mathbf{k}}) \geq 0$.

where $\hat{\mathbf{k}}$ is the unit basis vector pointing "up" from the domain D. Notice that $L(\mathbf{x}, t)$ simply gives the "signed distance" from $\mathbf{x}$ to the nearest point on the LCS. If moving along the curve $\mathbf{c}(s)$ in the positive $\mathbf{c}'(s)$ direction, then at least locally, points on the right have a positive value of L, and points on the left a negative value. Also note that the LCS is trivially given by the zero set $L = 0$.

4.2. Properties

There may exist points in the domain which have multiple possible values for $\mathbf{x_q}$. However, by the following theorem, we can always find an open set, $\mathcal{U}_t$, which contains the LCS and excludes any of these points.

Theorem 4.1. *Let $\mathcal{B} \subset D$ be the set of points with non-unique $\mathbf{x}_q$. This set is at a strictly positive distance from $\mathbf{c}(s)$.*

Proof. Since the curve $\mathbf{c}(s)$ is C^2 in s by Theorem 2.1, its curvature must remain finite. We will first show that $\mathcal{B}$ must be at a finite distance from $\mathbf{c}(s)$ by contradiction. Suppose that the set $\mathcal{B}$ is not a finite distance from $\mathbf{c}(s)$. In this case, we can find a sequence $\mathbf{x}_n \in \mathcal{B}$ such that $\mathbf{x}_n \to \mathbf{p} \in \mathbf{c}(s)$. By definition of $\mathcal{B}$, for each $\mathbf{x}_n$, there exist at least two points $\mathbf{x}_n^{(1)}$ and $\mathbf{x}_n^{(2)}$ on $\mathbf{c}(s)$ that are equidistant from $\mathbf{x}_n$ and every other point on the LCS is located at the same distance from $\mathbf{x}_n$ as these points or further. Since the curve $\mathbf{c}(s)$ is an injection, there are unique $s_n^{(1)}$ and $s_n^{(2)}$ such that $\mathbf{c}(s_n^{(1)}) = \mathbf{x}_n^{(1)}$ and $\mathbf{c}(s_n^{(2)}) = \mathbf{x}_n^{(2)}$.

Notice that

$$\|\mathbf{x}_n - \mathbf{p}\| \xrightarrow[n\to\infty]{} 0 \tag{36}$$

and

$$\|\mathbf{x}_n^{(1)} - \mathbf{x}_n\| = \|\mathbf{x}_n^{(2)} - \mathbf{x}_n\| \leq \|\mathbf{p} - \mathbf{x}_n\|, \tag{37}$$

so we must have

$$\left.\begin{aligned} &\mathbf{x}_n^{(1)} \xrightarrow[n\to\infty]{} \mathbf{p}, \\ &\mathbf{x}_n^{(2)} \xrightarrow[n\to\infty]{} \mathbf{p}, \\ &\mathbf{x}_n^{(1)} \neq \mathbf{x}_n^{(2)} \quad \text{for all } n. \end{aligned}\right\} \tag{38}$$

This allows us to define the curvature at $\mathbf{p}$ as the limit of the difference between the normal vectors at points $\mathbf{x}_n^{(1)}$ and $\mathbf{x}_n^{(2)}$. Let us denote by $\hat{\mathbf{n}}_n^{(1)}$ and $\hat{\mathbf{n}}_n^{(2)}$ the unit vectors normal to $\mathbf{c}(s)$ at respectively $\mathbf{x}_n^{(1)}$ and $\mathbf{x}_n^{(2)}$, cf. Fig. 2(a). The curvature κ is defined as the norm of the derivative with respect to s of the normal vector.

From Eq. (38), we get

$$\kappa(\mathbf{p}) = \lim_{n\to\infty} \left\| \frac{\hat{\mathbf{n}}_n^{(2)} - \hat{\mathbf{n}}_n^{(1)}}{s_n^{(2)} - s_n^{(1)}} \right\|. \tag{39}$$

Since $\kappa(\mathbf{p})$ is bounded due to the fact that $\mathbf{c}(s)$ is C^2, the limit of the right-hand side of Eq. (39) must remain bounded. We will show that if $\mathcal{B}$ is not at a finite distance from $\mathbf{c}(s)$, then this limit goes unbounded, providing the contradiction.

Notice that the points $\mathbf{x}_n^{(1)}$ and $\mathbf{x}_n^{(2)}$ are the points on $\mathbf{c}(s)$ that are the closest to $\mathbf{x}_n$, hence the vectors $\mathbf{x}_n^{(1)} - \mathbf{x}_n$ and $\mathbf{x}_n^{(2)} - \mathbf{x}_n$ must be *tangent* to respectively $\hat{\mathbf{n}}_n^{(1)}$ and $\hat{\mathbf{n}}_n^{(2)}$. Therefore the difference between the normal vectors can be written

$$\|\hat{\mathbf{n}}_n^{(2)} - \hat{\mathbf{n}}_n^{(1)}\| = \left\| \frac{\mathbf{x}_n^{(2)} - \mathbf{x}_n}{\|\mathbf{x}_n^{(2)} - \mathbf{x}_n\|} - \frac{\mathbf{x}_n^{(1)} - \mathbf{x}_n}{\|\mathbf{x}_n^{(1)} - \mathbf{x}_n\|} \right\| = \frac{\|\mathbf{x}_n^{(2)} - \mathbf{x}_n^{(1)}\|}{\|\mathbf{x}_n^{(2)} - \mathbf{x}_n\|}. \tag{40}$$

We also have that there exists some $D_p \in \mathbb{R}$ such that

$$\|\mathbf{c}'(s_{\mathbf{p}})\| = \lim_{n\to\infty} \frac{\|\mathbf{x}_n^{(2)} - \mathbf{x}_n^{(1)}\|}{|s_n^{(2)} - s_n^{(1)}|} = D_p > 0, \tag{41}$$

because the ridge is C^1 and $\mathbf{c}'(s) \neq 0$, so there is an n^* such that for all $n > n^*$,

$$\frac{\|\mathbf{x}_n^{(2)} - \mathbf{x}_n^{(1)}\|}{|s_n^{(2)} - s_n^{(1)}|} \geq \frac{D_p}{2} > 0, \tag{42}$$

by definition of the limit.

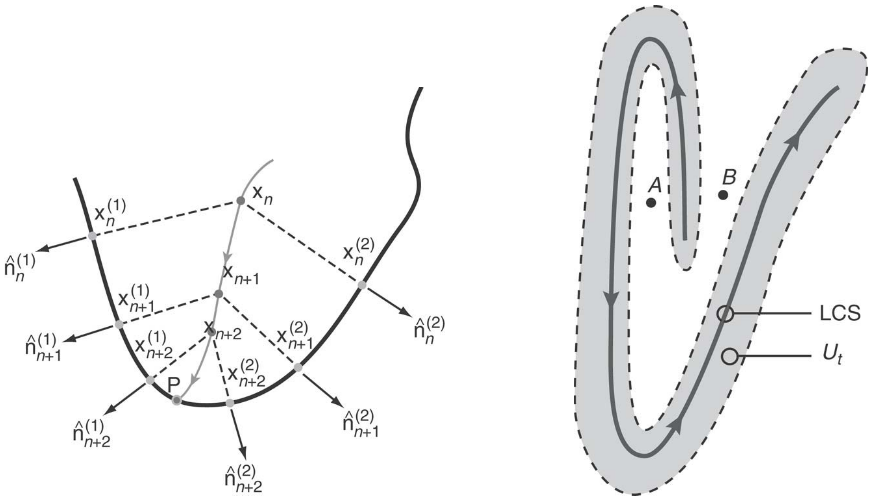

(a) Setting for the proof of Theorem 4.1.

(b) A tube $\mathcal{U}_t$ enclosing the LCS, where L is C^2.

Fig. 2. For an LCS represented as a curve $\mathbf{c}(s)$, we can always find an open set containing it that excludes points of discontinuity of L. In Panel (b), notice that even though for points **A** and **B** there are multiple values of $\mathbf{x_q}$ defined, the function $L(x, t)$ is still continuous at point **A**, however ∇L is not continuous at **A**.

Eqs. (39), (40) and (42) give

$$\kappa(\mathbf{p}) = \lim_{n\to\infty} \frac{1}{\|\mathbf{x}_n^{(2)} - \mathbf{x}_n\|} \frac{\|\mathbf{x}_n^{(2)} - \mathbf{x}_n^{(1)}\|}{|s_n^{(2)} - s_n^{(1)}|} \geq \frac{D_p}{2} \lim_{n\to\infty} \frac{1}{\|\mathbf{x}_n^{(2)} - \mathbf{x}_n\|} = +\infty, \tag{43}$$

which contradicts the fact that $\mathbf{c}(s)$ has a finite curvature at point $\mathbf{p}$. □

The theorem above allows us to define an open set $\mathcal{U}_t$ that completely contains the LCS. The fact that each $\mathbf{x} \in \mathcal{U}_t$ has a unique $\mathbf{x}_q$, allows us to show that the function L must be C^2 on and near the LCS.

Theorem 4.2. *$L(x, t)$ is C^2 over the open set $\mathcal{U}_t$.*

Proof. Since

$$L(\mathbf{x}, t) = \pm\|\mathbf{x} - \mathbf{x}_q\|, \tag{44}$$

we have

$$\nabla L = \frac{\pm 1}{\|\mathbf{x} - \mathbf{x}_q\|} \left\langle I - \frac{\mathrm{d}\mathbf{x}_q}{\mathrm{d}\mathbf{x}}, \mathbf{x} - \mathbf{x}_q \right\rangle. \tag{45}$$

However,

$$\left\langle \frac{\mathrm{d}\mathbf{x}_q}{\mathrm{d}\mathbf{x}}, \mathbf{x} - \mathbf{x}_q \right\rangle = 0 \tag{46}$$

in $\mathcal{U}_t$ because the closest point on the LCS does not change with variations in the direction normal to the curve. As a result,

$$\nabla L = \frac{\mathbf{x} - \mathbf{x}_q}{\pm\|\mathbf{x} - \mathbf{x}_q\|} = \frac{\mathbf{x} - \mathbf{x}_q}{L} = \hat{\mathbf{n}}(\mathbf{x}, t), \tag{47}$$

where we have used the fact that $\mathbf{x}_q$ is the point on the LCS closest to $\mathbf{x}$, hence $\hat{\mathbf{n}}(\mathbf{x}, t)$ must be parallel to $\mathbf{x} - \mathbf{x}_q$. Recall that there is a unique $\mathbf{x}_q$ for each $\mathbf{x} \in \mathcal{U}_t$, by virtue of Theorem 4.1. As a result, $\hat{\mathbf{n}}(\mathbf{x}, t)$ is a well-defined function of $\mathbf{x}$. Moreover, $\mathbf{c}(s)$ is C^2 by Theorem 2.1. This implies that $\mathbf{c}'(s)$ is C^1, and hence so is $\nabla L = \hat{\mathbf{n}} = \hat{\mathbf{k}} \times \mathbf{c}'/\|\mathbf{c}'\|$ since $\mathbf{c}' \neq 0$. □

Define the unit vector $\hat{\mathbf{t}}$, orthogonal to $\hat{\mathbf{n}}$ by $\hat{\mathbf{t}} = \hat{\mathbf{k}} \times \hat{\mathbf{n}}$. Notice that $\hat{\mathbf{t}}$ and $\hat{\mathbf{n}}$ are defined everywhere in $\mathcal{U}_t$, not just on the LCS. On the LCS, $\hat{\mathbf{t}}$ and $\hat{\mathbf{n}}$ correspond to, respectively, the tangent and orthogonal directions to the LCS. Therefore, on the LCS, $\hat{\mathbf{t}}$ is parallel to $\nabla\sigma$. But since $\nabla\sigma$ can be oriented either along $\dot{\mathbf{c}}(s)$ or $-\dot{\mathbf{c}}(s)$ and can even vanish, we prefer to use $\hat{\mathbf{t}}$ on the ridge instead of $\nabla\sigma$.

Let $\mathcal{L}$ be the Hessian of L and note the following properties of $\mathcal{L}$ and Σ:

Lemma 4.1. *Σ and $\mathcal{L}$ are self-adjoint.*

Proof. This result holds due to the symmetry of mixed partials. From $\Sigma(\mathbf{u}, \mathbf{v}) = \Sigma(\mathbf{v}, \mathbf{u})$, we deduce immediately that $\langle \mathbf{u}, \Sigma\mathbf{v}\rangle = \langle \mathbf{v}, \Sigma\mathbf{u}\rangle = \langle \Sigma\mathbf{u}, \mathbf{v}\rangle$ because the derivatives are necessarily real numbers. □

Theorem 4.3. *For $L = 0$, we have $\langle \hat{\mathbf{t}}, \Sigma\hat{\mathbf{n}}\rangle = \langle \hat{\mathbf{n}}, \Sigma\hat{\mathbf{t}}\rangle = 0$.*

Proof. From Definition 2.2, **SR2** implies that $\nabla L = \hat{\mathbf{n}}$ is an eigenvector of Σ. Hence, $\langle \hat{\mathbf{t}}, \Sigma\hat{\mathbf{n}}\rangle = \lambda_{\min}(\Sigma)\langle \hat{\mathbf{t}}, \hat{\mathbf{n}}\rangle = 0$, where $\lambda_{\min}(\Sigma)$ is the smallest eigenvalue of Σ. □

Corollary 4.1. *For $L = 0$ and an arbitrary vector $\mathbf{v}$, we have $\langle \hat{\mathbf{n}}, \Sigma\mathbf{v}\rangle = \langle \hat{\mathbf{n}}, \Sigma\hat{\mathbf{n}}\rangle\langle \hat{\mathbf{n}}, \mathbf{v}\rangle$.*

Proof. Developing $\mathbf{v}$ in the orthonormal basis $(\hat{\mathbf{t}}, \hat{\mathbf{n}})$ gives

$$\mathbf{v} = \langle \hat{\mathbf{t}}, \mathbf{v}\rangle\hat{\mathbf{t}} + \langle \hat{\mathbf{n}}, \mathbf{v}\rangle\hat{\mathbf{n}}. \tag{48}$$

Computing $\langle \hat{\mathbf{n}}, \Sigma\mathbf{v}\rangle$ in this basis and applying Theorem 4.3 gives the desired result. □

Lemma 4.2. *$\mathcal{L}\hat{\mathbf{n}} = 0$ everywhere in $\mathcal{U}_t$.*

Proof. Everywhere in $\mathcal{U}_t$, L is C^2, so the gradient ∇L exists and is differentiable. In particular, $\|\nabla L\| = 1$, therefore

$$0 = \nabla(\|\nabla L\|^2) = 2\mathcal{L}\nabla L = 2\mathcal{L}\hat{\mathbf{n}}. \quad \square \tag{49}$$

Lemma 4.3. *On the LCS, i.e., for $L = 0$,*

$$\langle \hat{\mathbf{n}}, \Sigma\hat{\mathbf{n}}\rangle \frac{\partial L}{\partial t} = \frac{\partial \langle \hat{\mathbf{n}}, \nabla\sigma\rangle}{\partial t}. \tag{50}$$

Proof. Take $\mathbf{x}$ on the LCS at time t, i.e., $L(\mathbf{x}, t) = 0$. Define $\mathbf{y} = \mathbf{x} + \alpha(\delta t)\hat{\mathbf{n}}$ such that $L(\mathbf{y}, t + \delta t) = 0$. In other words, $\mathbf{y}$ is at the intersection of the LCS at time $t + \delta t$ and the line starting at $\mathbf{x}$, orthogonal to the LCS at time t (see Fig. 3). Since we require $\mathbf{y} = \mathbf{x}$ for $\delta t = 0$, it follows that $\alpha(\delta t)$ is $\mathcal{O}(\delta t)$. Expanding L to second order in δt gives the following (where all derivatives on the right-hand side of Eqs. (51)–(59) are evaluated at $\mathbf{x}$ and t unless otherwise specified):

$$0 = L(\mathbf{y}, t + \delta t) = L(\mathbf{x}, t) + \alpha + \frac{\partial L}{\partial t}\delta t + \mathcal{O}(\delta t^2), \tag{51}$$

$$= \alpha + \frac{\partial L}{\partial t}\delta t + \mathcal{O}(\delta t^2). \tag{52}$$

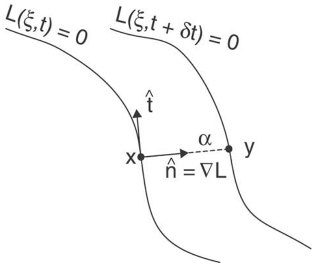

Fig. 3. Geometry of quantities discussed in Lemma 4.3.

Therefore,

$$\alpha = -\frac{\partial L}{\partial t}\delta t + \mathcal{O}(\delta t^2). \tag{53}$$

Now expanding ∇L, and plugging in Lemma 4.2, gives

$$\nabla L|_{\mathbf{y},t+\delta t} = \nabla L + \frac{\partial \nabla L}{\partial t}\delta t + \mathcal{O}(\delta t^2). \tag{54}$$

Taylor expanding $\nabla\sigma|_{\mathbf{y},t+\delta t}$ gives

$$\nabla\sigma|_{\mathbf{y},t+\delta t} = \nabla\sigma + \alpha\Sigma\hat{\mathbf{n}} + \frac{\partial\nabla\sigma}{\partial t}\delta t + \mathcal{O}(\delta t^2). \tag{55}$$

From Eqs. (47) and (53) we have

$$\nabla\sigma|_{\mathbf{y},t+\delta t} = \nabla\sigma - \frac{\partial L}{\partial t}\Sigma\nabla L\delta t + \frac{\partial\nabla\sigma}{\partial t}\delta t + \mathcal{O}(\delta t^2). \tag{56}$$

Since $\mathbf{y}$ is on the LCS at time $t+\delta t$, we must have

$$0 = \langle \nabla L|_{\mathbf{y},t+\delta t}, \nabla\sigma|_{\mathbf{y},t+\delta t}\rangle \tag{57}$$

$$= \langle \nabla L, \nabla\sigma\rangle + \delta t\left(-\frac{\partial L}{\partial t}\langle\nabla L, \Sigma\nabla L\rangle + \frac{\partial\langle\nabla L, \nabla\sigma\rangle}{\partial t}\right) + \mathcal{O}(\delta t^2) \tag{58}$$

$$= \delta t\left(-\langle\hat{\mathbf{n}}, \Sigma\hat{\mathbf{n}}\rangle\frac{\partial L}{\partial t} + \frac{\partial\langle\hat{\mathbf{n}}, \nabla\sigma\rangle}{\partial t}\right) + \mathcal{O}(\delta t^2). \tag{59}$$

Hence, we get the desired result, since δt is arbitrary. □

As stated above, and derived in the next section, the flux over the LCS, i.e., the level set $L=0$, is given by

$$\Phi(t) = \int_{\mathrm{LCS}} \frac{\mathrm{d}L}{\mathrm{d}t}\mathrm{d}s. \tag{60}$$

The next theorem provides an expression for $\mathrm{d}L/\mathrm{d}t$ based on quantities defining the FTLE and velocity fields.

Theorem 4.4. *Along the set $L=0$, we have*

$$\frac{\mathrm{d}L}{\mathrm{d}t} = \frac{\langle\hat{\mathbf{t}}, \nabla\sigma\rangle}{\langle\hat{\mathbf{n}}, \Sigma\hat{\mathbf{n}}\rangle}\left\langle\hat{\mathbf{t}}, \frac{\partial\hat{\mathbf{n}}}{\partial t} - J\hat{\mathbf{n}}\right\rangle + \mathcal{O}(1/|T|). \tag{61}$$

Proof. Lemma 4.3 gives

$$\langle \hat{\mathbf{n}}, \Sigma\hat{\mathbf{n}}\rangle \frac{\mathrm{d}L}{\mathrm{d}t} = \frac{\partial\langle \hat{\mathbf{n}}, \nabla\sigma\rangle}{\partial t} + \langle \hat{\mathbf{n}}, \Sigma\hat{\mathbf{n}}\rangle\langle \hat{\mathbf{n}}, \mathbf{v}\rangle. \tag{62}$$

Applying Corollary 4.1 and the chain rule for the derivative gives

$$\langle \hat{\mathbf{n}}, \Sigma\hat{\mathbf{n}}\rangle \frac{\mathrm{d}L}{\mathrm{d}t} = \left\langle \nabla\sigma, \frac{\partial\hat{\mathbf{n}}}{\partial t}\right\rangle + \left\langle \hat{\mathbf{n}}, \frac{\partial\nabla\sigma}{\partial t}\right\rangle + \langle \hat{\mathbf{n}}, \Sigma\mathbf{v}\rangle. \tag{63}$$

Using Corollary 3.1 in Eq. (63) gives

$$\langle \hat{\mathbf{n}}, \Sigma\hat{\mathbf{n}}\rangle \frac{\mathrm{d}L}{\mathrm{d}t} = \left\langle \nabla\sigma, \frac{\partial\hat{\mathbf{n}}}{\partial t} - J\hat{\mathbf{n}}\right\rangle + \mathcal{O}(1/|T|) \tag{64}$$

and the result follows by noticing that, for $L = 0$, the vector $\hat{\mathbf{t}}$ is proportional to $\nabla\sigma$, hence $\nabla\sigma = \langle \hat{\mathbf{t}}, \nabla\sigma\rangle\hat{\mathbf{t}}$. □

4.3. *Analysis*

Now we are in the position to analyze the flux across the LCS. Recall that

$$L(\mathbf{x}(t), t) = \pm\|\mathbf{x}(t) - \mathbf{x}_q(\mathbf{x}(t), t)\|,$$

where we have indicated the explicit functional dependencies of each variable. Therefore we have

$$\frac{\mathrm{d}L}{\mathrm{d}t} = \frac{\partial L}{\partial \mathbf{x}} \cdot \frac{\mathrm{d}\mathbf{x}}{\mathrm{d}t} + \frac{\partial L}{\partial \mathbf{x_q}} \cdot \frac{\mathrm{d}\mathbf{x}_q}{\mathrm{d}t}. \tag{65}$$

However,

$$\frac{\partial L}{\partial \mathbf{x_q}} = \frac{\mathbf{x}_q - \mathbf{x}}{L} = -\nabla L,$$

and so

$$\frac{\mathrm{d}L}{\mathrm{d}t} = \nabla L \cdot \left(\frac{\mathrm{d}\mathbf{x}}{\mathrm{d}t} - \frac{\mathrm{d}\mathbf{x}_q}{\mathrm{d}t}\right). \tag{66}$$

On the LCS, the two points $\mathbf{x}$ and $\mathbf{x}_q$ are equal; however, we think of $\mathbf{x}$ as being a *Lagrangian*, or material, point while $\mathbf{x}_q$ is viewed as a point which moves with the LCS. Notice the right-hand side of Eq. (66) represents the difference in the velocity of the two points, projected in the direction normal to the LCS. This projected difference in velocities is precisely what contributes to particles crossing the LCS. Therefore, the total flux across the LCS is given by

$$\Phi(t) = \int_{\mathrm{LCS}} \frac{\mathrm{d}L}{\mathrm{d}t}\mathrm{d}s, \tag{67}$$

where the integral is taken over the length of the LCS. Of course $\mathrm{d}L/\mathrm{d}t$, which is not directly obtainable, is to be replaced by its value given in Eq. (61), which can be computed from the FTLE field. If we normalize by the length of the LCS, we can define the *average escape rate* as

$$\eta(t) = \frac{\Phi(t)}{\int_{\mathrm{LCS}} \mathrm{d}s}. \tag{68}$$

Now we analyze the terms in the right-hand side of Eq. (61), starting first with the factor

$$\frac{\langle \hat{\mathbf{t}}, \nabla\sigma\rangle}{\langle \hat{\mathbf{n}}, \Sigma\hat{\mathbf{n}}\rangle}. \tag{69}$$

Recall that all terms in Eq. (61) are evaluated along the LCS. The numerator of Eq. (69) can be rewritten as $\langle \hat{\mathbf{t}}, \nabla\sigma\rangle = \|\nabla\sigma\|$. For time-independent flows, σ is constant along trajectories (asymptotically). Hence for any ridge in the FTLE field, $\nabla\sigma = 0$ along the ridge, and therefore the flux is zero. This is expected since for time-independent flows, streamlines and trajectories coincide. Experience dictates that even for highly time-dependent flows the value of σ does not vary much along ridges in the FTLE field and hence we can expect this term to typically be quite small. More precisely though, taking the derivative in the orthogonal direction (i.e., $\langle \hat{\mathbf{n}}, \nabla\|\nabla\sigma\|\rangle$) reveals that the numerator in Eq. (69) is indeed a minimum on the LCS.

Referring to Definition 2.2, we notice that the denominator of Eq. (69) is less than zero and is locally minimized (i.e., its norm is maximized). Therefore, for a well-defined ridge, we expect the magnitude of this term to be large, with a larger value the sharper the ridge. Since the numerator of Eq. (69) is locally minimized and the magnitude of the denominator is locally maximized, this implies that the magnitude of the factor given in Eq. (69) is locally minimized in the direction normal to the LCS, hence this multiplying factor is expected to be small for well-defined ridges.

Now consider the term

$$\left\langle \hat{\mathbf{t}}, \frac{\partial\hat{\mathbf{n}}}{\partial t} - J\hat{\mathbf{n}}\right\rangle \tag{70}$$

from Eq. (61). The quantity $\langle \hat{\mathbf{t}}, \frac{\partial\hat{\mathbf{n}}}{\partial t}\rangle$ represents how fast the LCS is locally rotating, which we think of as a *Lagrangian* rotation. This is easily seen since, for an appropriate θ, we can write $\hat{\mathbf{n}} = (\cos\theta, \sin\theta)$ and $\hat{\mathbf{t}} = (-\sin\theta, \cos\theta)$ so

$$\left\langle \hat{\mathbf{t}}, \frac{\partial\hat{\mathbf{n}}}{\partial t}\right\rangle = \begin{bmatrix} -\sin\theta & \cos\theta \end{bmatrix} \begin{bmatrix} -\dot{\theta}\sin\theta \\ \dot{\theta}\cos\theta \end{bmatrix} = \dot{\theta},$$

which is the local rotation rate of the LCS. Now notice $J\hat{\mathbf{n}}$ is the linearized velocity field applied to a unit vector normal to the LCS; and taking the inner product of this with the tangent to the LCS, $\hat{\mathbf{t}}$, gives the component in the direction of the LCS. That is, the term $\left\langle \hat{\mathbf{t}}, J\hat{\mathbf{n}}\right\rangle$ measures how much the local Eulerian field rotates vectors normal to the LCS. We therefore view this term as a local *Eulerian* rotation rate and hence Eq. (70) is a local measure of *the difference in the rotation rate of the LCS from the rotation rate induced by the (instantaneous) velocity field*.

If the linearized flow about the LCS turns at a sufficiently uniform speed, then the LCS will follow that rotation. On the other hand, if there is a sudden increase or decrease of the local vorticity in the field (i.e., a short-term error or a short-term vortex), the LCS may become less Lagrangian. In the second example studied below, we extract a strong LCS from high-frequency radar data near the coast of Florida. Small vortices in the domain can be observed and eventually degrade the LCS, as observed by Lekien et al. [23].

The last term in the right-hand side of Eq. (61) scales inversely to the integration time. Notice that, if $T \to 0$, then the FTLE is an instantaneous, or Eulerian, measure of separation, which is often not very enlightening for aperiodic systems [11]. However, for T finite, we obtain a Lagrangian measure of separation because the FTLE considers the integrated effect of the flow over the interval T. Thus the $\mathcal{O}(1/T)$ term in Eq. (61) which states that the LCS becomes more Lagrangian as T increases should seem reasonable. However, it is important to keep in mind that, based on the time scales of the system dynamics, ridges in the FTLE field can become more or less pronounced as T increases; that is, the term given by Eq. (69) can become smaller *or* larger as T increases even though the $\mathcal{O}(1/T)$ term in Eq. (61) is tending to zero. This is because for aperiodic flows, strongly hyperbolic lines can lose their hyperbolicity as time evolves, or restating, some LCSs exist only over strictly finite-time intervals. So for example, as T initially is increased a ridge (LCS) in the FTLE field may sharpen, but as T extends beyond

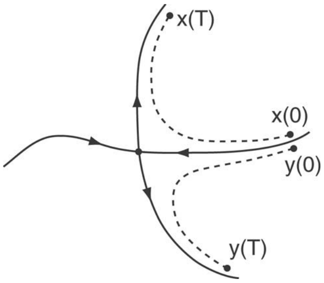

Fig. 4. Two points on either side of a stable manifold will diverge after a sufficient amount of time.

the interval of existence of the LCS, the ridge may disappear. The next section and [21] include discussion about choosing T.

5. Computation of FTLE and LCS

This section provides an overview of the numerical computation of FTLE and LCS and some computational concerns. All too often theoretical ideas are demonstrated through numerical examples without properly explaining the computational method, which can be troublesome if two methods can produce dramatically different results. This development helps bridge the gap between the above theoretical development and the results shown in the following example sections.

The algorithm starts with the computation of the flow map, the map that takes an initial fluid particle position $\mathbf{x}_0$ at time t to its later position $\mathbf{x}(t+T;t,\mathbf{x}_0)$ at time $t+T$. To perform this analysis, a grid of particles is launched at time t; in the examples below, a Cartesian mesh is used. Each particle is advected with a fourth-order Runge–Kutta–Fehlberg algorithm integrating either analytic velocity data, or discrete velocity field data. For discrete velocity data, a third-order interpolator [22] was used. Once the final positions, $\mathbf{x}(t+T;t,\mathbf{x}_0)$, of each particle are found, the spatial gradient of the flow map can be evaluated at each point in the **initial** grid by finite differencing with values at the neighboring grid points [13,23]. Once the gradient of the flow map is computed, obtaining the FTLE at each point is a straightforward evaluation of Eq. (12). This procedure is then repeated for a range of times t to provide a time-series of FTLE fields.

By finite differencing neighboring points in the grid, the gradient of the flow map (and hence the FTLE) is being approximated, or smoothed out. However, this smoothing is often desirable in obtaining rough approximations to the locations of LCSs. For example, consider a generic hyperbolic point and its stable and unstable manifolds as shown in Fig. 4. The hyperbolicity of the fixed point should cause two points on either side of the stable manifold to diverge after a sufficient amount of time T; therefore we can expect high FTLE values along the stable manifold. But since the value of the FTLE can quickly decrease away from the manifold, it is possible that the *theoretical* FTLE values at $\mathbf{x}(0)$ and $\mathbf{y}(0)$ can be both quite low if the gradient of the flow map is computed from truly infinitesimal differencing. However, if the derivative of the flow map at point $\mathbf{x}(0)$ is computed by differencing with the trajectory of $\mathbf{y}(0)$ (or vice versa), then the *computed* value will be large since these points straddle the stable manifold (i.e., LCS). Therefore, if we only know the theoretical FTLE values over a coarse grid, one would not likely see any ridges in the FTLE field since we cannot expect grid points to lie on, or sufficiently close to, the LCS. However, by differencing the computational grid as outlined above, LCSs that lie between grid points should still be revealed, even for relatively coarser meshes.

An analysis of the influence of the integration time T in the computation of FTLE fields can be found in [21]. Roughly speaking, as T increases, more of the LCS becomes resolved; for example if in Fig. 4 the two points started further to the right then they would need a longer T to separate. For most practical applications the dynamical system is only known over a finite time interval, or over a finite domain, and hence T is typically bounded by the availability of data. While locating LCS is not particularly sensitive to T, choosing the optimal value for a given application is not always obvious.

To extract the LCS from FTLE fields, both the Hessian of the FTLE field and the gradient lines are determined. In the case of a Cartesian grid, the Hessian is easily computed from finite-differencing. The gradient field can be found by Morse–Smale decomposition. Once the eigenvectors corresponding to the minimum eigenvalue direction of the Hessian are computed, a scalar field can be formed by taking the inner product of these eigenvectors with the gradient field. Then ridges are extracted by looking at the zero-valued level sets.

Notice that $\hat{\mathbf{t}} \cdot \nabla\sigma$ is used in Eq. (61) instead of equivalently using $\|\nabla\sigma\|$. This is for numerical purposes. The norm of the gradient can increase rapidly if we are slightly off the ridge because the curvature has been maximized, so $\hat{\mathbf{t}} \cdot \nabla\sigma$ should be less sensitive to numerical errors on the position of the ridge.

6. Example 1: Analytical model of a double-gyre flow

In this section we apply some of the preceding results to a periodically varying double-gyre. This flow is described by the stream-function

$$\psi(x, y, t) = A\sin(\pi f(x, t))\sin(\pi y), \tag{71}$$

where

$$f(x, t) = a(t)x^2 + b(t)x, \tag{72}$$

$$a(t) = \epsilon\sin(\omega t), \tag{73}$$

$$b(t) = 1 - 2\epsilon\sin(\omega t), \tag{74}$$

over the domain [0, 2] × [0, 1]. This model should not be seen as the approximate solution to a real fluid flow, but rather a simplification of a double-gyre pattern that occurs frequently in geophysical flows [4,24]. The analytical forms of the parameters in Eq. (74) were chosen to produce a simple time-dependent flow with fixed boundaries, not to approach a solution of Navier–Stokes' equation.

The velocity field is given by

$$u = -\frac{\partial\psi}{\partial y} = -\pi A\sin(\pi f(x))\cos(\pi y), \tag{75}$$

$$v = \frac{\partial\psi}{\partial x} = \pi A\cos(\pi f(x))\sin(\pi y)\frac{\mathrm{d}f}{\mathrm{d}x}. \tag{76}$$

For $\epsilon = 0$ the flow is time-independent and has the same pattern as Fig. 5(a). However, for $\epsilon \neq 0$ the flow is time-dependent and the gyres conversely expand and contract periodically in the x-direction such that the rectangle enclosing the gyres remains invariant. In Eq. (71), A determines the magnitude of the velocity vectors, $\omega/2\pi$ is the frequency of oscillation, and ϵ is *approximately* how far the line separating the gyres moves to the left or right, that is, the amplitude of the motion of the separation point $\tilde{x}$ on the x axis about the point $(1, 0)$ is

$$\begin{aligned}\tilde{x} - 1 &= \frac{\sqrt{1 + 4\epsilon^2\sin^2(\omega t)} - 1}{2\epsilon\sin(\omega t)}\\ &\approx \frac{1 + 2\epsilon^2\sin^2(\omega t) - 1}{2\epsilon\sin(\omega t)}, \qquad \text{for small } \epsilon\\ &= \epsilon\sin(\omega t).\end{aligned} \tag{77}$$

Fig. 5 shows the velocity field of the periodic double-gyre at various times for $A = 0.1$, $\omega = 2\pi$, and $\epsilon = 0.25$. Notice that the period of motion is equal to 1 for this case, hence at time 0 both gyres are equal in size, at time 0.25

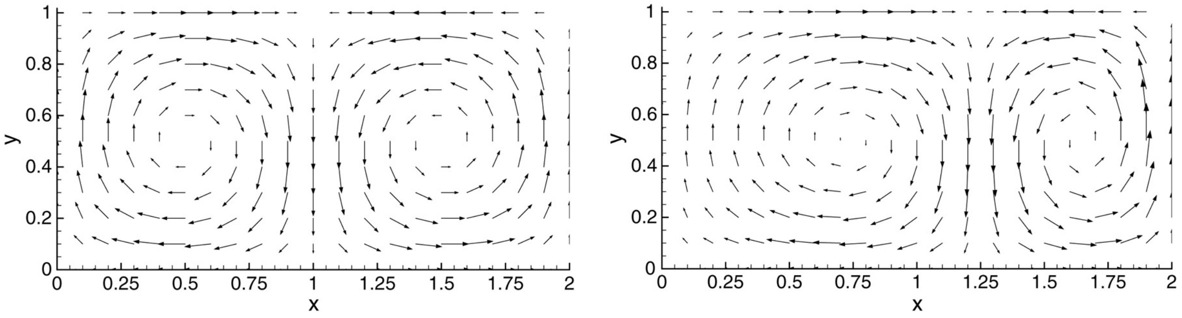

(a) $t = 0$, $t = 0.5$, $t = 1$.

(b) $t = 0.25$.

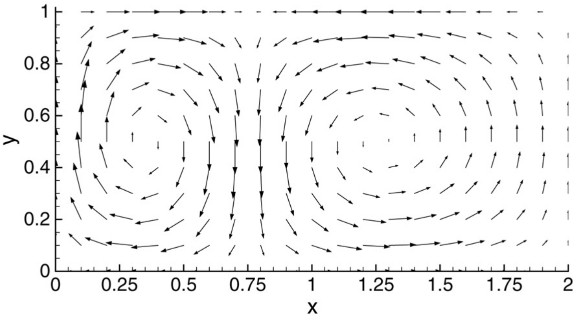

(c) $t = 0.75$.

Fig. 5. The double-gyre velocity field for $A = 0.1$, $\omega = 2\pi$, and $\epsilon = 0.25$ at several different times.

the line separating the gyres is offset furthest to the right a distance $\approx \epsilon$, at time 0.5 the line has returned to the middle, at time 0.75 the line is offset furthest to the left a distance $\approx \epsilon$, and at time 1 the velocity field completes one period.

For $\epsilon = 0$ the system can be thought of as a time-independent 2-D Hamiltonian system. For this case there is a heteroclinic connection of the unstable manifold of the fixed point $(1, 1)$ with the stable manifold of the fixed point $(1, 0)$. The FTLE field for the double-gyre flow is shown in Fig. 6(a) for $\epsilon = 0$. The LCS, indicated by a line of high FTLE, represents this heteroclinic connection, which in this case is an invariant manifold.

For $\epsilon \neq 0$, but small, we can think of the system as perturbed from the time-independent case. We might expect this perturbation to cause a classic entanglement of the unstable and stable manifolds [8,41]. This is exactly what is indicated by the plot of the FTLE field for the system with $\epsilon = 0.1$, which is shown in Fig. 6(b). Notice the LCS which extends from the bottom of the domain and loops back and forth near the top. The integration time used for Fig. 6(b) was $T = 1.5$ periods. If the integration is extended in time, further looping would be revealed. If the integration were carried out in backward time, i.e., $T < 0$, one would see an LCS extending from the top of the domain and analogously looping back and forth near the bottom of the domain. It should be noted that Fig. 6(b) shows the FTLE computed from the flow map and not for a Poincaré map.

6.1. *Flux over the LCS*

Here we show that the LCS in Fig. 6(b) is indeed nearly Lagrangian. In Fig. 7(a) we have highlighted the LCS shown in the FTLE field of Fig. 6(b) and used an **X** to represent a Lagrangian tracer which is located on the LCS at time $t = 0$. Fig. 7(b)–(d) show the location of the LCS and the tracer at later times. From this plot, the LCS is

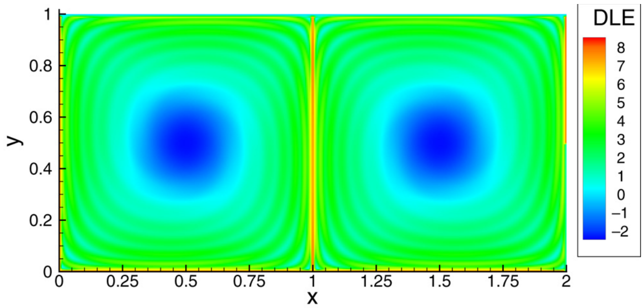

(a) $\epsilon = 0$.

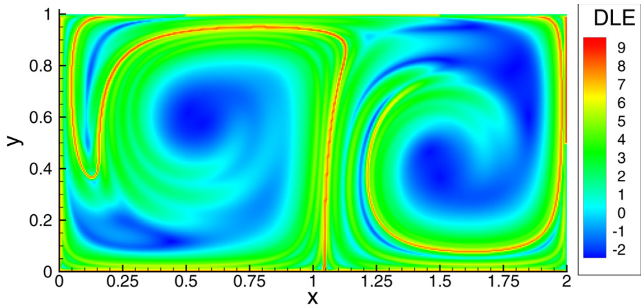

(b) $\epsilon = 0.1$.

Fig. 6. FTLE plots for the double-gyre flow for $t = 0$. In both cases, $A = 0.1$. For the time-dependent case, shown in Panel (b), $\omega = 2\pi/10$, and $T = 15$. (For interpretation of the references to colour in this figure legend, the reader is referred to the web version of this article.)

indistinguishably Lagrangian, that is, the tracer seems to move perfectly *along* the structure. However, if we refine the calculation, and take a closer look, we can see that there is a very slight flux across the LCS.

Fig. 8 shows a highly refined computation of the LCS and the location of the Lagrangian tracer. The grid spacing that was used for the computation of FTLE was 1×10^{-5}. Computations reveal that the tracer moves at an average rate of 5×10^{-5} normal to the LCS over the interval considered. This rate is about 0.05% of the magnitude of the velocity field in that region. It is important to note that this rate persists with further refinement of the computations.

To verify Theorem 4.4, the terms in the right-hand side of Eq. (61) were computed from a first-order approximation. The $\mathcal{O}(1/T)$ term dominates for this example with $1/T \approx 0.03$. This confirms Eq. (61) since the "directly computed" flux of 5×10^{-5} is well below $\mathcal{O}(1/T)$.

7. Example 2: VHF radar data off the coast of Florida

High-resolution ocean velocity data has become readily available since the introduction of Very High Frequency (VHF) radar technology. In this section, we use data collected along the Florida coast to compute the FTLE field and extract the LCS in this area. To validate Theorem 4.4, we compute the flux across the LCS using both a direct computation and an evaluation of the flux given in Eq. (61). We show that the rate at which particles cross the LCS is less than 0.05% of the average magnitude of the velocity field in the region. This confirms Theorem 4.4 and validates the fact that ridges in the FTLE field (that reveal the Lagrangian behavior of the flow) are also Lagrangian (i.e., their motion obeys the equation of motion of the fluid).

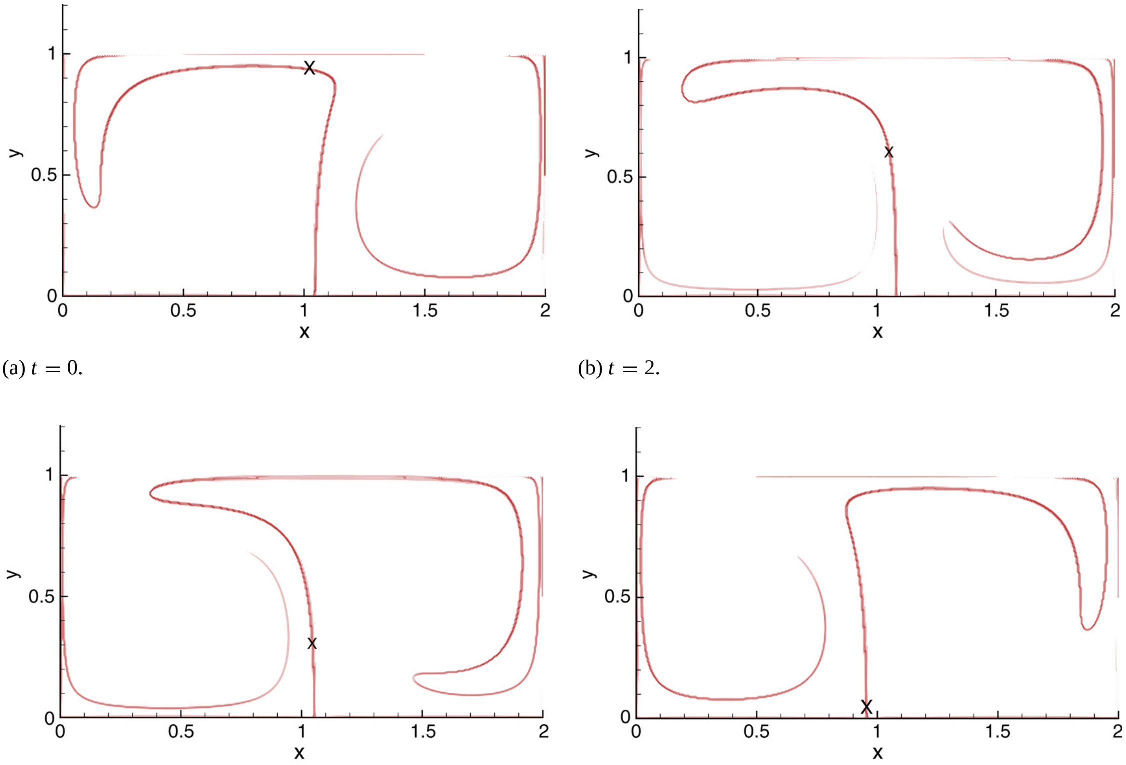

(a) $t = 0$.

(b) $t = 2$.

(c) $t = 3$.

(d) $t = 5$.

Fig. 7. Locations of the LCS and the Lagrangian tracer at four different times. The tracer is denoted by the **X** (Computed with $A = 0.1$, $\omega = 2\pi/10$, $\epsilon = 0.1$ and $T = 15$). (For interpretation of the references to colour in this figure legend, the reader is referred to the web version of this article.)

7.1. *Very high frequency radar data*

The use of radio frequencies to measure ocean surface currents has received attention in recent coastal oceanographic experiments [46,37,43]. The Ocean Surface Current Radar (OSCR) VHF system was deployed for the Southern Florida Ocean Measurement Center (SFOMC) 4-Dimensional Current Experiment from June 25 through August 25, 1999. Recent observations of surface currents from OSCR using the VHF mode reveal complex flow patterns in this region. More details about the experimental setting and observations can be found in [44,45]. Data from the OSCR system represent coastal surface currents mapped over a 7 km × 8.5 km domain at 20 min intervals with a horizontal resolution of 250 m at 700 grid points. The map for July 22, 1999 12:00 GMT can be found in Panel (a) of Fig. 9.

7.2. *Direct Lyapunov exponents and LCS*

To compute the FTLE field using the VHF radar data, a uniform grid of 800 × 800 particles was used. The FTLE map for July 22, 1999 12:00 GMT can be found in Panel (b) of Fig. 9.

Notice that the domain depicted in Fig. 9 has an open-boundary. The computation of trajectories must be stopped if they exit the domain since velocity data does not extend through this region, and extrapolation would not be meaningful. Such trajectories are disregarded *when* they exit the domain and the FTLE is computed with a smaller integration time, equal to the time at which the trajectory exited.

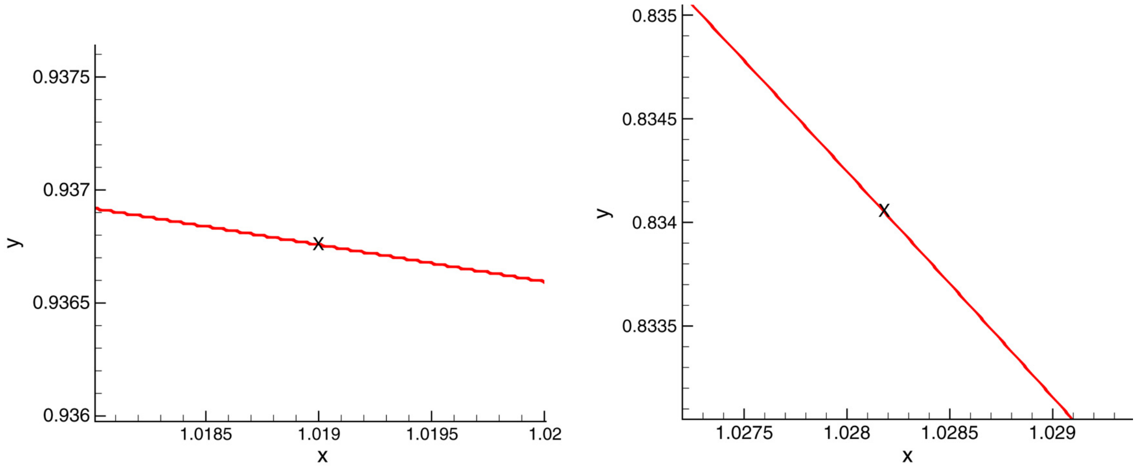

(a) $t = 0$.

(b) $t = 1$.

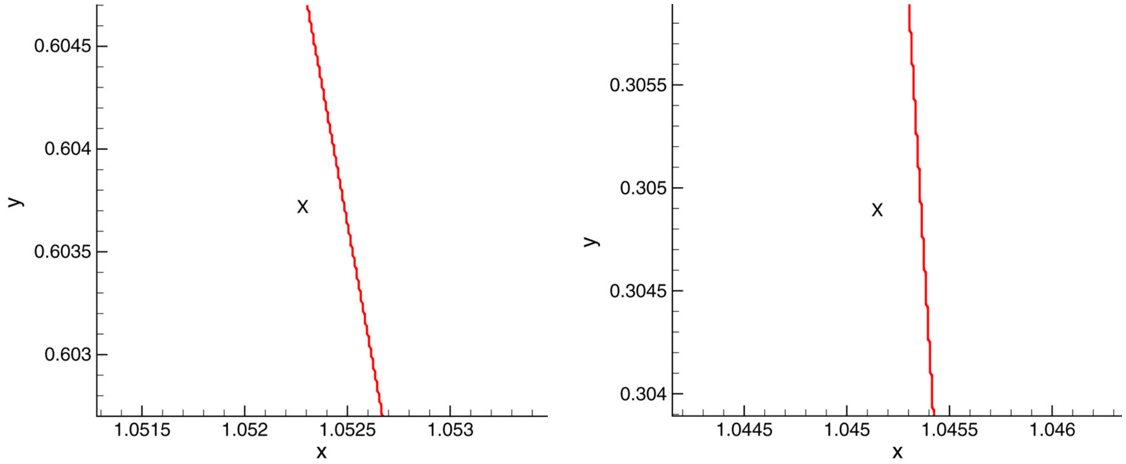

(c) $t = 2$.

(d) $t = 3$.

Fig. 8. Highly refined plots of the locations of the LCS and the Lagrangian tracer at four different times. (Computed with $A = 0.1$, $\omega = 2\pi/10$, $\epsilon = 0.1$, $T = 30$, and a grid spacing for FTLE computations of 10^{-5}.) (For interpretation of the references to colour in this figure legend, the reader is referred to the web version of this article.)

There is a noticeable ridge of high FTLE in Fig. 9(b) which encapsulates an LCS. Analysis of the motion of fluid parcels [23] reveals that any particle northeast of this structure is flushed out of the domain in only a few hours. In contrast, parcels starting southwest of the structure typically recirculate several times near the Florida coast before they finally rejoin the current. Interestingly, this unique behavior is not obvious from a simple observation of the velocity footprints—which are typically not very revealing for flows with general time dependence. However, the Lagrangian footprint of the LCS easily exposes this behavior.

7.3. LCS flux

The objective of this section is to show that for typical coastal flows, such as the one studied here, ridges of the FTLE field are nearly Lagrangian. For this purpose we computed the FTLE field at several instances in time

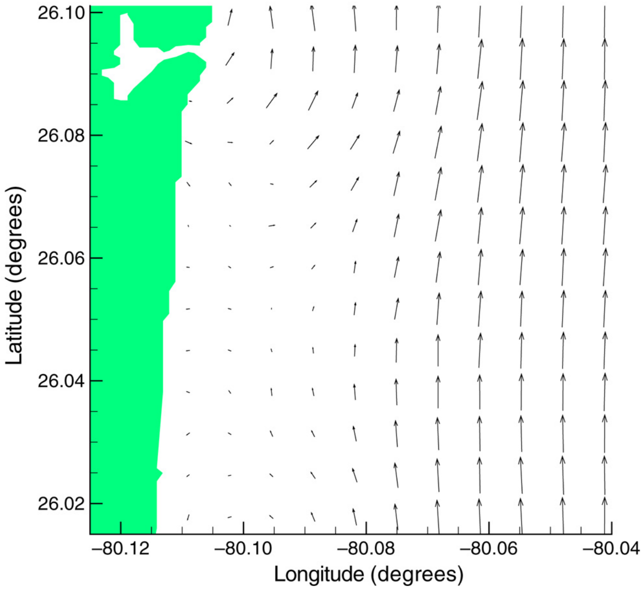

(a) Velocity field.

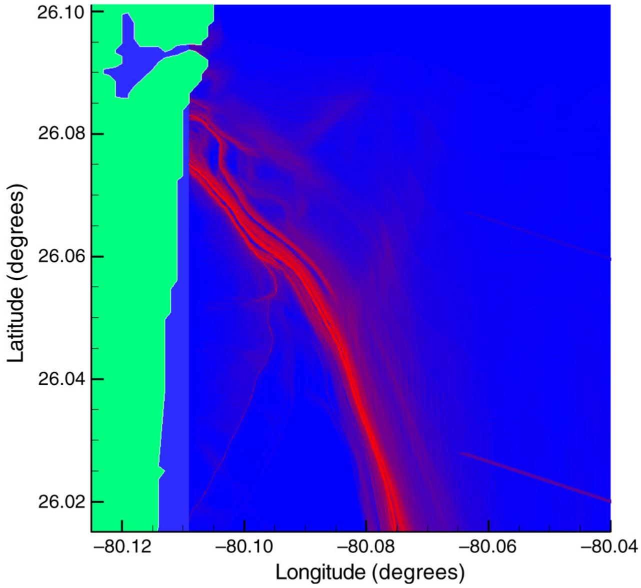

(b) FTLE field.

Fig. 9. Panel (a) shows a vector plot of the velocity field off the Florida coast as observed by the OSCR VHF system on July 22, 1999 12:00 GMT. Panel (b) shows the FTLE field for July 22, 1999 12:00 GMT, computed from OSCR data. The Florida coastline is located on the left and shaded green. The area shaded blue represents regions of low FTLE and the red represents high FTLE. (For interpretation of the references to colour in this figure legend, the reader is referred to the web version of this article.)

(Fig. 10). Fig. 11(a) shows the LCS extracted from the FTLE shown in Fig. 10 at several 30 min time steps starting with July 22, 1999 12:00 GMT. Each curve corresponds to the ridge $\mathbf{c}_{t_0+\tau}(s)$ extracted from the field $\sigma^{T}_{t_0+\tau}(\mathbf{x})$,

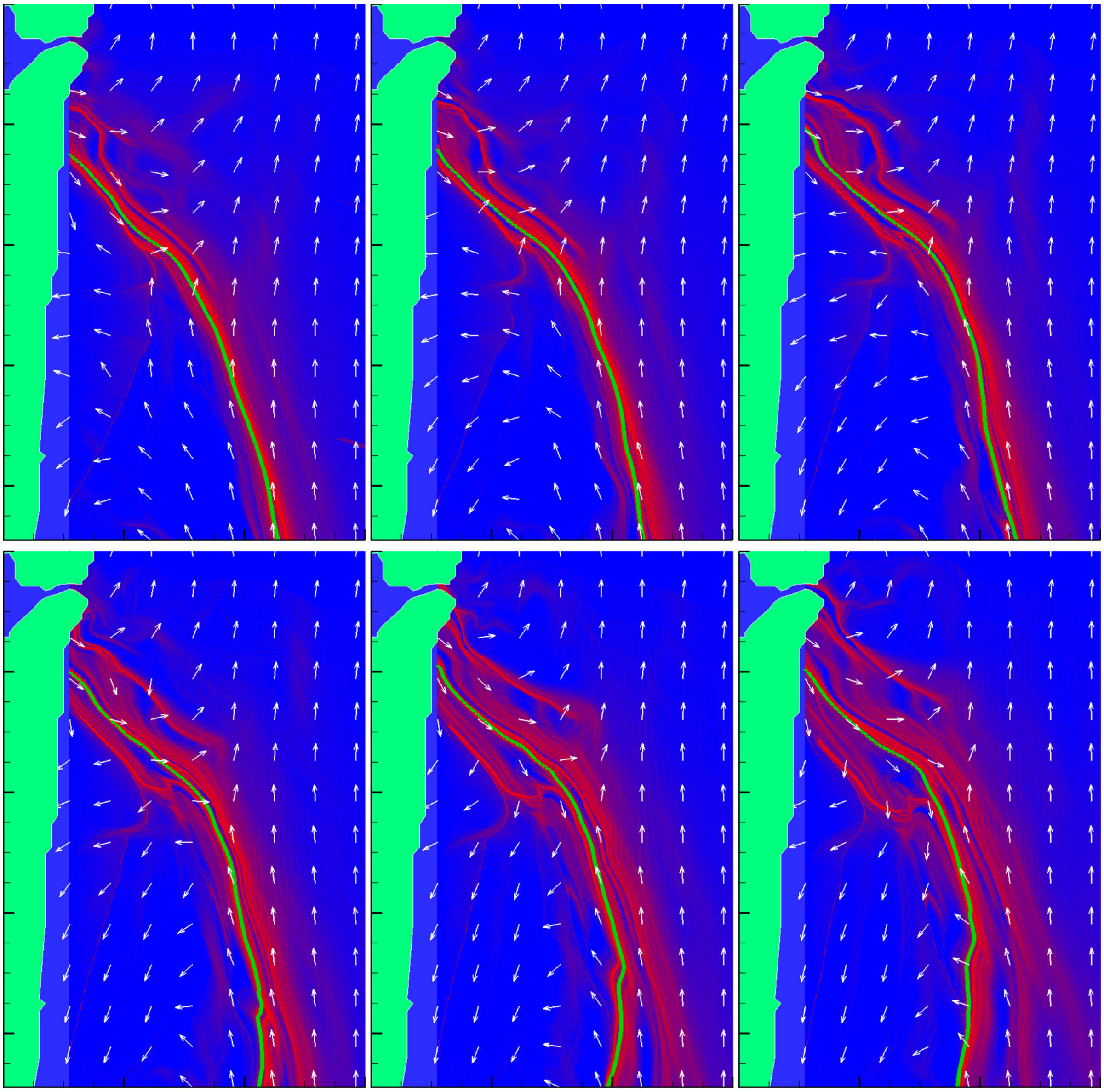

Fig. 10. From left to right and from top to bottom, FTLE field and LCS on July 22 12:00 GMT, 12:30 GMT, 13:00 GMT, 13:30 GMT, 14:00 GMT and 14:30 GMT. Superimposed on each plot is the Eulerian velocity field (using the same length for each vector) at the corresponding time. Fig. 11(a) shows these six LCS superimposed on a single frame. (For interpretation of the references to colour in this figure legend, the reader is referred to the web version of this article.)

where $T = 25$ h is constant, t_0 is set to July 22, 1999 12:00 GMT and τ increases from zero by increments of 30 min. Our goal is to show that $\mathbf{c}_{t_0+\tau}(s)$ is nearly identical to the integration *of the material line* $\mathbf{c}_{t_0}(s)$ from t_0 to $t_0 + \tau$.

Panel (a) of Fig. 12 shows a close-up of the successive locations of the LCS and the corresponding locations of the integrated material curve. To the naked eye, the LCS behaves as a Lagrangian line. A slight deviation can be

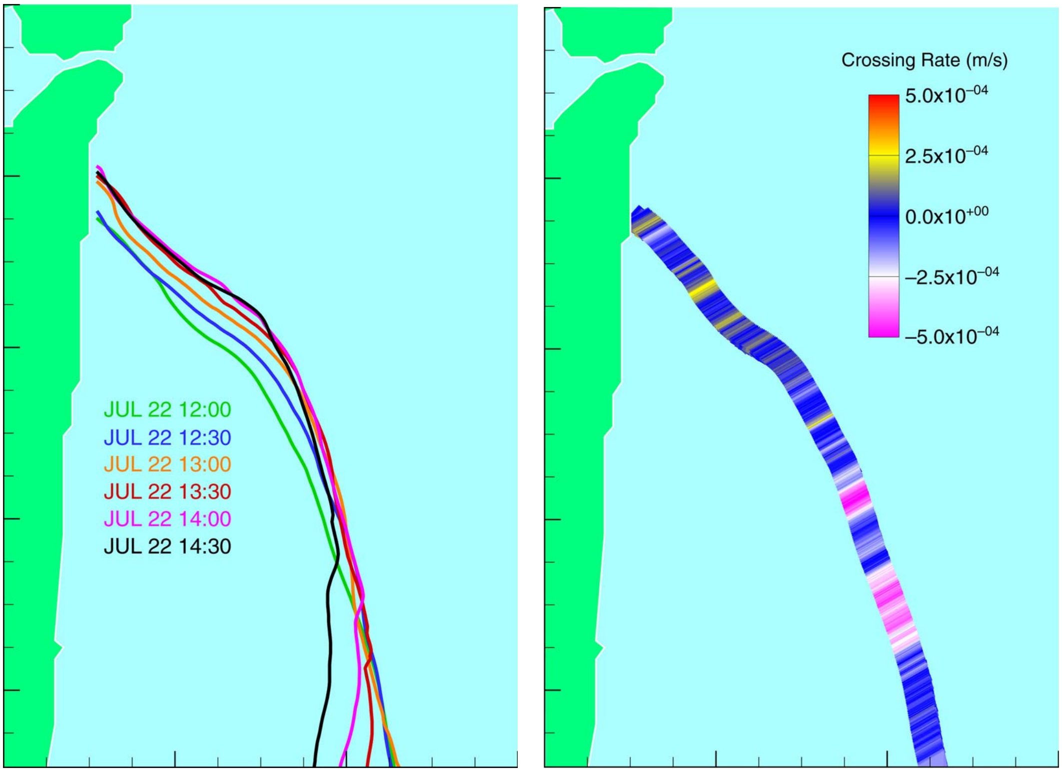

(a) LCS at 30 min intervals.

(b) Crossing rate.

Fig. 11. Panel (a) superimposes the locations of the LCS at six different times, spaced every 30 min. Panel (b) shows the instantaneous crossing rate along the LCS at July 22, 1999 12:00 GMT. (For interpretation of the references to colour in this figure legend, the reader is referred to the web version of this article.)

noticed after about three hours, but it is not possible to tell from this analysis if that discrepancy is due to numerical error or is inherent.

To give a more definitive and qualitative result, and verify Theorem 4.4, we need to compute the flux, or crossing rate, across the LCS. This is done “directly” by approximating the projected difference in velocity between the LCS and the material line using finite differencing. In other words, the LCS is computed for several times $t = t_0 + k\delta t$. In addition, we integrate the LCS computed at time t_0 from t_0 to t as if it was a line of fluid particles. The difference between the LCS at time t and the integrated line of fluid particles from t_0 to t gives the average flux between t_0 and t, where $t - t_0$ is the averaging time. As the averaging time goes to zero, i.e., $t \to t_0$, we expect the measured average flux to converge toward its instantaneous value $\Phi(t)$. The results of these computations are shown in Fig. 11(b) and Fig. 12(b).

Panel (b) of Fig. 11 shows the distribution of the crossing rate along the LCS computed for July 22, 1999 12:00 GMT. The bars and dashed line in Panel (b) of Fig. 12 represent the computed rate at which particles cross the LCS as a function of the averaging time. One can see that as the averaging time goes to zero, the rate converges to about 0.01 cm s^{-1}. The typical velocity of fluid particles is about 0.05 degrees min^{-1} or 30 cm s^{-1} in the vicinity of the LCS [33,45,23]. Therefore, the maximum compound flux along the LCS is less than 0.05% of the average speed of the flow in that region.

In addition to computing the flux directly, we evaluated the first-order term given by Eq. (61). This value is referred to as the “theoretical limit” on Panel (b) of Fig. 12. Notice that the theoretical limit is very close to the

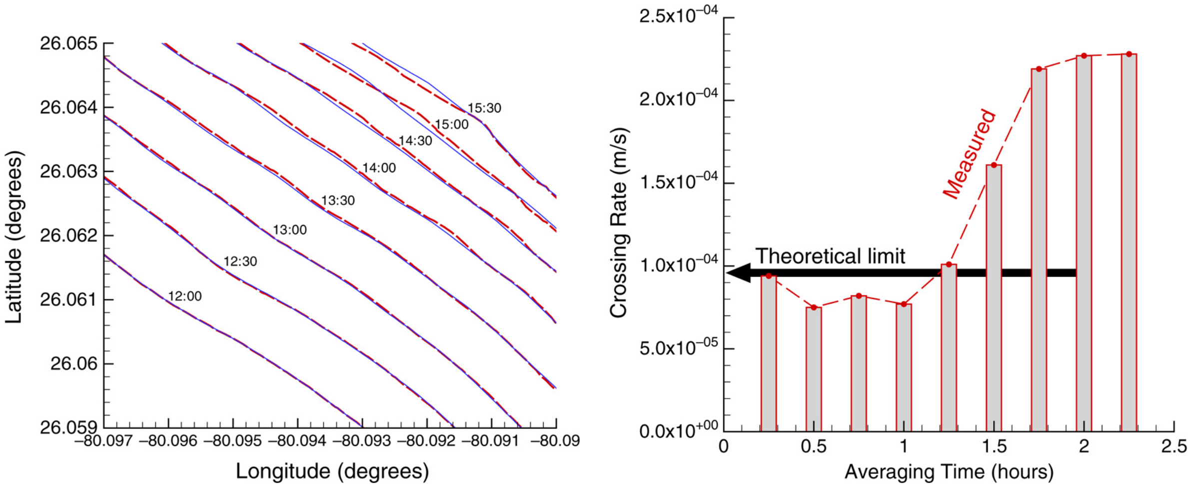

(a) LCS and material line at 30 min intervals.

(b) Crossing rate averaged over time.

Fig. 12. Panel (a) shows a comparison between the location of the LCS, $\mathbf{c}_{t+\tau}(s)$ at different increments of times, τ, (solid blue curves) with the location of the advected material line, which initially corresponds to $\mathbf{c}_t(s)$ (dashed red curves). Panel (b) shows the average crossing rate along the LCS as a function of time; notice that the limiting value for the flux is 10^{-4} m/s. (For interpretation of the references to colour in this figure legend, the reader is referred to the web version of this article.)

limit of the average flux for $t \to t_0$. This suggest that the integration time T is long enough for the term $\mathcal{O}(1/|T|)$ in Eq. (61) to be negligible.

As an example of how short-term vorticity can break down LCS, we note that during the SFOMC experiment surface current observations revealed Florida Current intrusions over the shelf break, wavelike structures along the inshore edge of the current, and numerous sub-mesoscale vortices [44]. One example started at 01:20 GMT on June 26, 1999, when a sub-mesoscale vortex was located along the southern part of the VHF-radar domain just inshore of the Florida Current. Surface currents within the vortex ranged from 20–30 cm s^{-1} at a diameter of about 1–1.25 km from the vortex's center. The vortex's northward displacement of about 6 km occurred over a 5 h period. While there is a continuous presence of distinct, slowly-rotating LCSs in the domain, the eddies moving North collide with the structures and eventually break them down by adding local vorticity [23].

8. Example 3: Separation over an airfoil

In this example we show the utility of computing LCSs from FTLE fields to obtain the unsteady separation profile of flow over an airfoil. Haller [15] recently derived a criterion for the existence of separation profiles in unsteady flows. In this section, we show that the existence of such a Lagrangian profile is indicated by a Lagrangian ridge in the FTLE field. The geometry of the airfoil is known as GLAS-II and has been used in the area of active flow control where an oscillatory blowing valve is placed on the surface of the airfoil to provide regulated pressure oscillations by means of blowing or suction. This enables control of the separation and reattachment points over the airfoil, and hence control of aerodynamic properties such as lift and drag.

The velocity data used to compute FTLE was provided by a viscous vortex method [3,6,7]. Fig. 13 shows the FTLE field for two different times. There is a noticeable LCS attached to the rear of the airfoil.

In Fig. 14 we have plotted the evolution of the FTLE field together with a grid of fluid particles. In these plots, however, the FTLE is plotted by a color contour plot in which only high values of FTLE are shaded and low values are masked by shading them white. This allows us to highlight the ridge of high FTLE (i.e., the LCS) and keep the

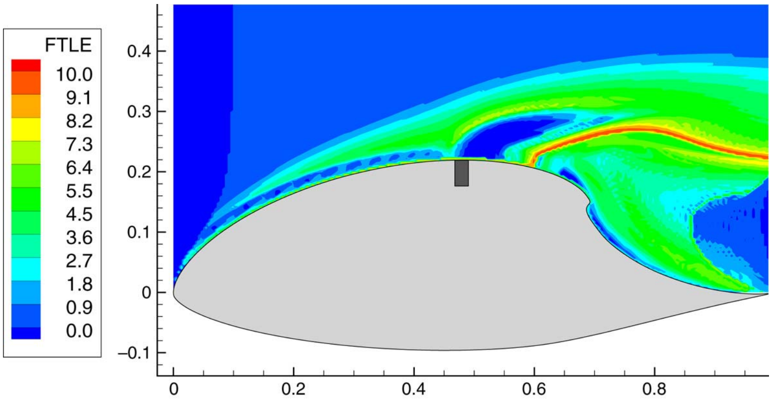

(a) $t = 0.0$.

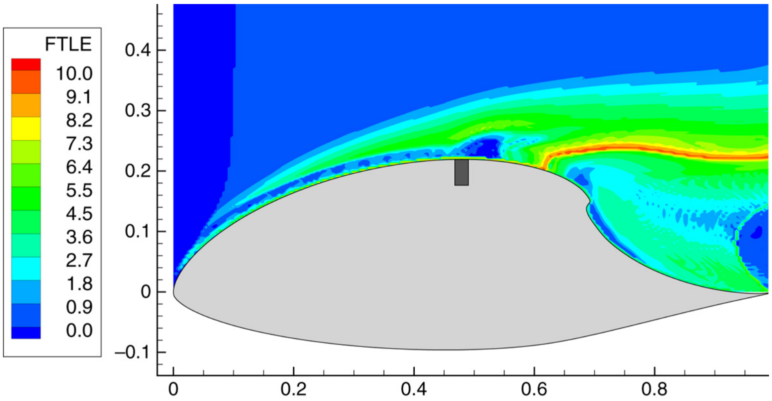

(b) $t = 3.2$.

Fig. 13. FTLE field on the airfoil at different times. A moving LCS following the separation profile is clearly visible. For the complete movie see http://www.lekien.com/~francois/papers/qLCS. (For interpretation of the references to colour in this figure legend, the reader is referred to the web version of this article.)

rest of the plot transparent. This LCS reveals the separation profile which separates the free-stream flow over the airfoil from the separation bubble or dead-water zone.

An unsteady separation profile can be thought of as a material line that attracts and ejects particles near the separation point [51,15]. Therefore, the separation profile behaves like an unstable manifold. As previously mentioned, for time-independent systems stable manifolds produce ridges in the FTLE field when computed using a positive integration time, $T > 0$, and unstable manifolds are revealed from backward integration, $T < 0$. Therefore, the FTLE fields shown in Fig. 14 were computed from *integrating backward in time*. To obtain the FTLE field at time t, a grid of particles is advected from time t to time $t - |T|$ (or equivalently $t + T$ where $T < 0$). Once the FTLE has been computed in this manner for a series of times t, the forward time evolution of the LCS can then be presented by sequentially showing these fields as t increases.

To demonstrate the Lagrangian behavior of the LCS, a uniform grid of fluid particles is placed in the flow at time $t = 0$. To aid in the visualization, particles are shaded differently based on their initial location relative to the LCS. Note that the trajectory of these particles was *not* used to compute the FTLE, since these particles are being advected *forward* in time. The location of the blowing valve is denoted by the dark gray rectangle located on the top, center of the airfoil in Fig. 14. The flow is actuated to produce a highly unsteady separation point.

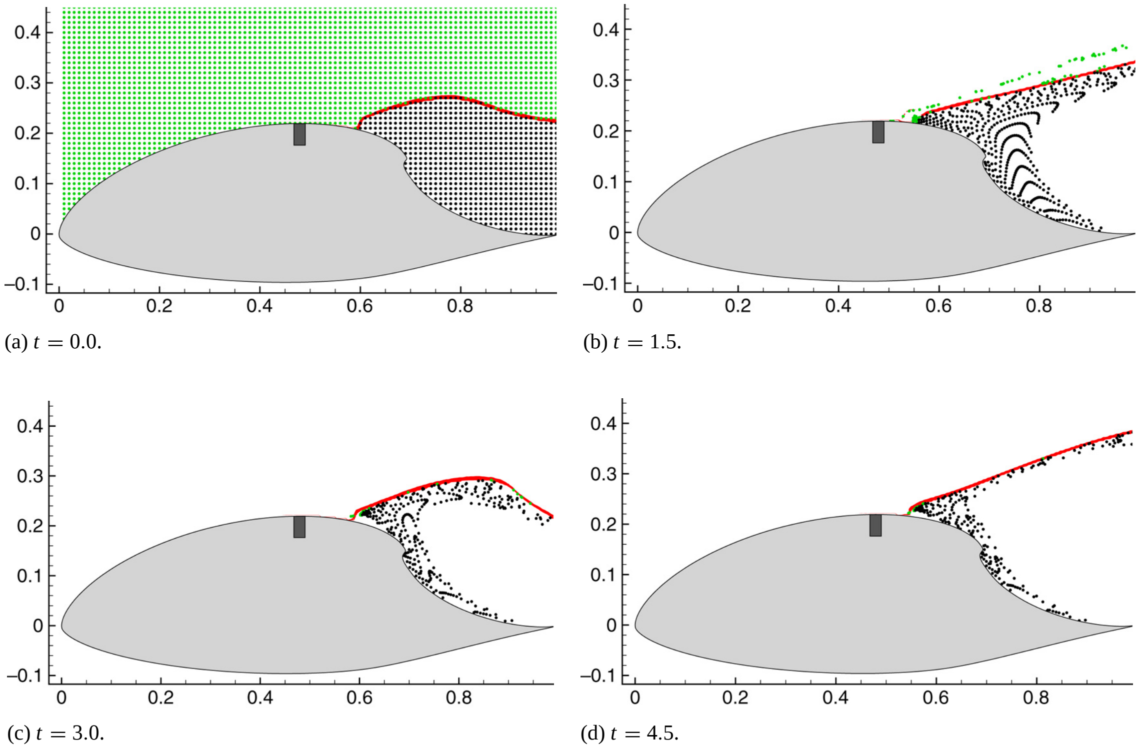

(a) $t = 0.0$.

(b) $t = 1.5$.

(c) $t = 3.0$.

(d) $t = 4.5$.

Fig. 14. Evolution of an LCS, given by the red curve, and a grid of fluid particles over time. Particles initially located above the LCS are colored green, while particles initially located below the LCS are colored black. In this example, the LCS represents a separation profile that marks the boundary between the free-stream flow from the dead-water zone behind the airfoil, for the complete movie see http://www.lekien.com/˜francois/papers/qLCS. (For interpretation of the references to colour in this figure legend, the reader is referred to the web version of this article.)

As we can see from Fig. 14, even though the LCS is itself highly unsteady, it does a remarkable job capturing not just a transport barrier between the two regions, but the actual separation profile. Particles located above the LCS exit the domain very quickly with the ones locally near the LCS being ejected along the structure, while particles below the LCS are slowly ejected along the LCS. For the complete animation of Fig. 14, see http://www.lekien.com/˜francois/papers/qLCS.

Note that this example demonstrates that prediction of *future* Lagrangian behavior can be obtained from FTLE fields obtained by integrating *backward in time*, e.g., predicting the qualitative behavior of particles based on their initial location with respect to the LCS. It should also be noted that the assumption listed in Eq. (14) is not satisfied at the separation point because the velocity field has a no-slip boundary condition along the surface of the airfoil. However, as this simulation shows, extrapolation of the LCS to the boundary appears to be reasonable for practical purposes.

9. Conclusions

The study of transport barriers in systems with general time dependence, especially those given by a finite set of data, is often best accomplished by studying finite-time Lyapunov exponent fields. Lagrangian coherent structures are defined as ridges in the FTLE field. These structures can help reveal the mixing and transport geometry of a system. The study of LCS for general time-dependent systems, such as the ocean, is often analogous to studying the stable and unstable manifolds of time-independent or time-periodic dynamical systems. LCS typically represent separatrices which divide the flow into dynamically distinct regions.

The *traditional* Lyapunov exponent (limiting value of the FTLE as $T \to \infty$) gives a measure of the ergodicity of the flow and is often used as a statistical measure of the steady state. So even for chaotic flows, such as in Section 6, the Lyapunov exponent may become uniform over the domain, but over a finite time interval, FTLE fields give a clear description of the mixing geometry over the time scales considered. Therefore FTLE fields are able to capture the transient behavior of a system, which is most significant for general aperiodic systems where LCSs can exist on a variety of time scales.

The precise definition of LCS presented in this paper is based on an idea proposed by Haller [12,14]. Although the FTLE has previously been used to extract LCSs in the study of various dynamical systems [34,35,49,50,23,24,17], a refined definition was needed to provide a more rigorous framework for the study of the Lagrangian properties. The definition presented in this paper allows for the analysis and proof of Lagrangian properties, and supports the computation and numerical extraction of LCSs from data sets.

An expression for the flux over an LCS was derived in Theorem 4.4, for which it was shown that for well-defined LCSs, or those able to rotate with the local Eulerian field, there is a negligible amount of flux, which is inversely proportional to the integration time of the FTLE.

The theoretical results presented in this paper were verified for two applications: an analytical double-gyre and observational data of surface currents off the coast of Florida. In both examples, the flux across the LCS was less than 0.05% of the average magnitude of the velocity field near the LCS. In addition, a third application was presented, which showed the ability of FTLE fields to capture unsteady separation profiles in flow over an airfoil. These examples reaffirmed that ridges in the FTLE field, i.e., LCSs, are indeed Lagrangian.

Acknowledgments

This work has profited from the motivation and support of the Adaptive Ocean Sampling Network (AOSN) team as well as the Adaptive Sampling and Prediction (ASAP) team.

The authors are grateful to Naomi Leonard for her valuable support and greatly thank George Haller for his helpful remarks and enlightening discussions. We also thank Rouslan Krechetnikov for his valuable suggestions.

Numerical results in this paper were produced using MANGEN (http://www.mangen.info), a software package developed by Francois Lekien and Chad Coulliette at the California Institute of Technology and supported by Program Manager Manuel Fiadeiro at the Office of Naval Research. The authors are grateful to Chad Coulliette for many enlightening and enjoyable discussions about coherent structures in geophysical flows.

The high-frequency radar data used was collected by the Rosentiel School of Marine and Atmospheric Science (RSMAS) at the University of Miami. The authors are grateful to Arthur Mariano, Edward Ryan and Lynn Shay for sharing their results and their experience in using experimentally measured footprints in Lagrangian studies.

The authors would also like to sincerely thank Jeff Eldredge for providing the velocity data for the flow around the airfoil in Section 8.

This research was partially supported by ONR grants N00014-02-1-0826 and N00014-04-1-0534. Shawn Shadden is supported by a National Science Foundation fellowship.

References

[1] L. Barreira, Y. Pesin, Lyapunov Exponents and Smooth Ergodic Theory, in: University Lecture Series, vol. 23, American Mathematical Society, Providence, RI, 2002.

[2] W.A. Coppel, Dichotomies in Stability Theory, in: Springer Lecture Notes in Mathematics, vol. 629, Springer-Verlag, New York, 1978.

[3] G.H. Cottet, P. Koumoutsakos, Vortex Methods: Theory and Practice, Cambridge University Press, 2000.

[4] C. Coulliette, S. Wiggins, Intergyre transport in a wind-driven, quasigeostrophic double gyre: An application of lobe dynamics, Nonlinear Process. Geophys. 7 (2000) 59–85.

[5] R. Doerner, B. Hübinger, W. Martienssen, A. Grossmann, S. Thomae, Stable manifolds and predictability of dynamical systems, Chaos Solitons Fractals 10 (11) (1999) 1759–1782.

[6] J.D. Eldredge, T. Colonius, A. Leonard, A vortex particle method for two-dimensional compressible flow, J. Comput. Phys. 179 (2002) 371–399.

[7] J.D. Eldredge, Efficient tools for the simulation of flapping wing flows, AIAA Paper 2005–0085.

[8] J. Guckenheimer, P. Holmes, Nonlinear Oscillations, Dynamical Systems and Bifurcations of Vector Fields, in: AMS, vol. 42, Springer-Verlag, New York, 1983.

[9] G. Haller, A.C. Poje, Finite-time transport in aperiodic flows, Physica D 119 (2000) 352–380.

[10] G. Haller, Lagrangian coherent structures and mixing in two-dimensional turbulence, Chaos 10 (1) (2000) 99–108.

[11] G. Haller, G. Yuan, Lagrangian coherent structures and mixing in two-dimensional turbulence, Physica D 147 (2000) 352–370.

[12] G. Haller, Distinguished material surfaces and coherent structures in 3d fluid flows, Physica D 149 (2001) 248–277.

[13] G. Haller, Lagrangian structures and the rate of strain in a partition of two-dimensional turbulence, Phys. Fluids A 13 (2001) 3368–3385.

[14] G. Haller, Lagrangian coherent structures from approximate velocity data, Phys. Fluids A 14 (2002) 1851–1861.

[15] G. Haller, Exact theory of unsteady separation for two-dimensional flows, J. Fluid Mech. 512 (2004) 257–311.

[16] P. Hartman, Ordinary Differential Equations, John Wiley and Sons, Inc., Baltimore, 1973.

[17] T. Inanc, S.C. Shadden, J.E. Marsden, Optimal trajectory generation in ocean flows, in: Proc. of 24th American Control Conference, Portland, USA, June 2005.

[18] C.K.R.T. Jones, S. Winkler, Invariant manifolds and Lagrangian dynamics in the ocean and atmosphere, in: B. Fiedler, G. Iooss, N. Kopell (Eds.), Handbook of Dynamical Systems II: Towards Applications, World Scientific, 2002, pp. 55–92.

[19] B. Joseph, B. Legras, Relation between kinematic boundaries, stirring, and barriers for the Antarctic polar vortex, J. Atmospheric Sci. 59 (2002) 1198–1212.

[20] T.-Y. Koh, B. Legras, Hyperbolic lines and the stratospheric polar vortex, Chaos 12 (2002) 382–394.

[21] F. Lekien, N. Leonard, Dynamically consistent Lagrangian coherent structures, in: American Institute of Physics: 8th Experimental Chaos Conference, vol. 742, 2004, pp. 132–139.

[22] F. Lekien, J. Marsden, Tricubic interpolation in three dimensions, Internat. J. Numer. Methods Engrg. 63 (3) (2005) 455–471.

[23] F. Lekien, C. Coulliette, A.J. Mariano, E.H. Ryan, L.K. Shay, G. Haller, J.E. Marsden, Pollution release tied to invariant manifolds: A case study for the coast of Florida, Physica D 210 (1–2) (2005) 1–20.

[24] F. Lekien, C. Coulliette, G. Haller, J. Paduan, J.E. Marsden, Optimal pollution release in Monterey Bay based on nonlinear analysis of coastal radar data, Environ. Sci. Technol. 2005 (under review).

[25] A.M. Liapunov, Stability of Motion, Academic Press, New York, 1966.

[26] N. Malhotra, I. Mezić, S. Wiggins, Patchiness: A new diagnostic for Lagrangian trajectory analysis in time-dependent fluid flows, Internat. J. Bifur. Chaos 8 (1998) 1073–1094.

[27] A.M. Mancho, S. Small, S. Wiggins, K. Ide, Computation of stable and unstable manifold of hyperbolic trajectories in two-dimensional, aperiodically time-dependent vector fields, Physica D 182 (2003) 188–222.

[28] J.E. Marsden, M.J. Hoffman, Elementary Classical Analysis, 2nd ed., W.H. Freeman and Company, New York, 1993.

[29] I. Mezic, S. Wiggins, A method for visualization of invariant sets of dynamical systems based on the ergodic partition, Chaos 9 (1) (1999) 213–218.

[30] B. O'Neill, Elementary Differential Geometry, 2nd ed., Academic Press, San Diego, 1997.

[31] V.I. Oseledec, A multiplicative ergodic theorem: Ljapunov characteristic numbers for dynamical systems, Trans. Moscow Math. Soc. 19 (1968) 197–231.

[32] J.M. Ottino, The Kinematics of Mixing: Stretching, Chaos, and Transport, Cambridge University Press, Cambridge, 1989.

[33] H. Peters, L.K. Shay, A.J. Mariano, T.M. Cook, Current variability on a narrow shelf with large ambient vorticity, J. Geophys. Res.-Oceans 107 (C8) (2002) art. no.–3087.

[34] R.T. Pierrehumbert, Large-scale horizontal mixing in planetary atmospheres, Phys. Fluids A 3 (5) (1991) 1250–1260.

[35] R.T. Pierrehumbert, H. Yang, Global chaotic mixing on isentropic surfaces, J. Atmospheric Sci. 50 (1993) 2462–2480.

[36] A.C. Poje, G. Haller, Geometry of cross-stream mixing in a double-gyre ocean model, J. Phys. Oceanogr. 29 (1999) 1649–1665.

[37] D. Prandle, The fine-structure of nearshore tidal and residual circulations revealed by HF radar surface current measurements, J. Phys. Oceanogr. 17 (1987) 231–245.

[38] A. Provenzale, Transport by coherent barotropic vortices, Annu. Rev. Fluid Mech. 31 (1999) 55–93.

[39] A. Rogerson, P.D. Miller, L.J. Pratt, C.K.R.T.J. Jones, Lagrangian motion and fluid exchange in a barotropic meandering jet, J. Phys. Oceanogr. 29 (10) (1999) 2635–2655.

[40] V. Rom-Kedar, Transport rates of a class of two-dimensional maps and flows, Physica D 43 (1990) 229–268.

[41] V. Rom-Kedar, A. Leonard, S. Wiggins, An analytical study of transport, mixing, and chaos in unsteady vortical flow, J. Fluid Mech. 214 (1990) 347–394.

[42] V. Rom-Kedar, S. Wiggins, Transport in two-dimensional maps: Concepts, examples, and a comparison of the theory of Rom-Kedar and Wiggins with the Markov model of Mackay, Meiss, Ott, and Percival, Physica D 51 (1991) 248–266.
[43] H.C. Shay, L.K. Graber, D.B. Ross, R.D. Chapman, Mesoscale ocean surface current structure detected by HF radar, J. Atmos. Ocean. Technol. 12 (1995) 881–900.
[44] L.K. Shay, T.M. Cook, B.K. Haus, J. Martinez, H. Peters, A.J. Mariano, P.E. An, S. Smith, A. Soloviev, R. Weisberg, M. Luther, VHF radar detects oceanic submesoscale vortex along the Florida coast, EOS Trans. Am. Geophys. Union 81 (19) (2000) 209–213.
[45] L.K. Shay, T.M. Cook, H. Peters, A.J. Mariano, R. Weisberg, P.E. An, A. Soloviev, M. Luther, Very high frequency radar mapping of the surface currents, IEEE J. Oceanogr. Engin. 27 (2002) 155–169.
[46] R.H. Stewart, J.W. Joy, HF radio measurements of surface currents, Deep-Sea Res. 21 (1974) 1039–1049.
[47] C.A. Truesdell, The Kinematics of Vorticity, Indiana University Press, Bloomington, 1954.
[48] F. Verhulst, Nonlinear Differential Equations and Dynamical Systems, 2nd ed., Springer-Verlag, New York, 1996.
[49] J. von Hardenberg, K. Fraedrich, F. Lunkeit, A. Provenzale, Transient chaotic mixing during a baroclinic life cycle, Chaos 10 (1) (2000) 122–134.
[50] G.A. Voth, G. Haller, J.P. Gollub, Experimental measurements of stretching fields in fluid mixing, Phys. Rev. Lett. 88 (25) (2002) 254501.1–254501.4.
[51] K.C. Wang, On current controversy of unsteady separation, in: Symposium on Numerical and Physical Aspects of Aerodynamic Flows, Long Beach, CA, January 19–21, 1981.
[52] S. Wiggins, Chaotic Transport in Dynamical Systems, Springer-Verlag, New York, 1992.
[53] S. Wiggins, The dynamical systems approach to Lagrangian transport in ocean flows, Annu. Rev. Fluid Mech. 37 (2005) 295–338.
[54] G.C. Yuan, L.J. Pratt, C.K.R.T Jones, Barrier destruction and Lagrangian predictability at depth in a meandering jet, Dyn. Atmos. Oceans 35 (1) (2002) 41–61.